The Astrophysical Journal, 665:369–389, 2007 August 10

OBSERVATIONAL CONSTRAINTS ON INTERSTELLAR GRAIN ALIGNMENT

B-G Andersson
Center for Astrophysical Sciences, Johns Hopkins University, Baltimore, MD 21218; bg@pha.jhu.edu

and

S. B. Potter
South African Astronomical Observatory, Observatory 7935, Cape Town, South Africa; sbp@saao.ac.za
Received 2006 September 21; accepted 2007 May 8

ABSTRACT

We present new multicolor photopolarimetry of stars behind the Southern Coalsack. Analyzed together with multiband polarization data from the literature, probing the Chamaeleon I, Musca, ρ Opiuchus, R CrA, and Taurus clouds, we show that the wavelength of maximum polarization ($\lambda_{\max}$) is linearly correlated with the radiation environment of the grains. Using far-infrared emission data, we show that the large scatter seen in previous studies of $\lambda_{\max}$ as a function of A_V is primarily due to line-of-sight effects causing some A_V measurements to not be a good tracer of the extinction (radiation field strength) seen by the grains being probed. The derived slopes in $\lambda_{\max}$ versus A_V, for the individual clouds, are consistent with a common value, while the zero intercepts scale with the average values of the ratios of total to selective extinction (R_V) for the individual clouds. Within each cloud we do not find direct correlations between $\lambda_{\max}$ and R_V. The positive slope is consistent with recent developments in theory and indicating alignment driven by the radiation field. The present data cannot conclusively differentiate between direct radiative torques and alignment driven by H_2 formation. However, the small values of $\lambda_{\max}(A_V = 0)$, seen in several clouds, suggest a role for the latter, at least at the cloud surfaces. The scatter in the $\lambda_{\max}$ versus A_V relation is found to be associated with the characteristics of the embedded YSOs in the clouds. We propose that this is partially due to locally increased plasma damping of the grain rotation caused by X-rays from the YSOs.

Subject headings: dust, extinction — ISM: individual (Southern Coalsack, Chamaeleon I, Musca, ρ Ophiuchus, R CrA, Taurus) — polarization

Online material: color figures, machine-readable tables

1. INTRODUCTION

Starlight seen through the interstellar medium usually ends up being slightly polarized (at the level of up to a few percent), even when the background source is not. This interstellar polarization was first detected independently by J. Hall and W. A. Hiltner (Hall 1949; Hiltner 1949a). Already Hiltner (1949b) suggested that the polarization was due to interstellar dust interacting with the magnetic field. Theoretical models attempting to explain interstellar polarization soon followed, with the first quantitative one by Davis & Greenstein (1951), who identified grain alignment by the magnetic field through paramagnetic dissipation as the origin of the polarization. This identification of dichroic extinction as the origin of the polarization has remained as the prime candidate up until this time, although the details of the mechanism have been modified by many authors over the intervening half-century (for a recent review see Lazarian 2003). For instance, while Davis & Greenstein (1951) assumed paramagnetic grains, spun up by gas-grain collisions, it is now recognized that this combination will not suffice to keep the grains spun up against the damping influence of those same gas-grain collisions. The grains have to either have a stronger magnetic moment (superparamagnetic grains; Mathis 1986) or be spun up to rotational velocities well above the thermal energy of the gas (suprathermal rotation; Purcell 1979).

The magnetic relaxation causing the rapidly spinning grain to align its axis of angular momentum with the local direction of the magnetic field is well understood and based on solid-state and nuclear physics (Purcell 1979; Lazarian & Draine 1999). The remaining poorly understood link in the explanatory chain to understand the origin of interstellar polarization is the mechanism of grain spin-up. Several mechanisms have been proposed on theoretical grounds, including the energy released from molecular hydrogen formation on the surface of the dust grain (Purcell 1979) and direct torques from an anisotropic radiation field (Dolginov & Mitrofanov 1976; Weingartner & Draine 2003; Cho & Lazarian 2005).

It is generally agreed that, for the large grains involved in the polarization, the damping of the grain spin, in neural gas, is due to gas-grain collisions (Draine & Lazarian 1998). For smaller grains or in regions with more extreme conditions, radiation from the grains or other collisional partners can dominate (Draine & Lazarian 1998). Even so, the grain neutral damping is often used as a benchmark. A damping time can be defined such that it corresponds to the time it takes for a grain to collide with its own mass in gas particles. If we define the effective radius, a, as that which a grain of a given volume would have if it were spherical, we find that (Whittet 1992)

$$t_{\rm damping} \propto \frac{a}{n\sqrt{T}}, \tag{1}$$

where n and T are the gas number density and temperature, respectively. Hence, smaller grains have their rotation damped out more rapidly and are therefore the hardest to keep spinning. A hotter and/or denser gas also dampens the grain rotation faster. Therefore, the size distribution of aligned grains can be used as a probe of the alignment mechanism.

The first attempts at determining the wavelength dependence of interstellar polarization (e.g., Hiltner 1949a) were inconclusive.

Davis & Greenstein (1951) made a qualitative prediction of the wavelength dependence of interstellar polarization, later expanded on by Davis (1959). Isolated single-wavelength observations hinting at such variations were indirectly reported by Strömgren in the 1954–1955 annual report of the Yerkes and McDonald Observatories, where he notes that Hiltner had made observations at 1 and 2 μm, showing a steep drop in polarization compared to "the blue" (Strömgren 1956). The first systematic attempt at measuring the "polarization curve" to be published was undertaken by A. Behr at Göttingen in 1958, at the prodding of L. Davis, Jr. (Behr 1959). While wavelength dependence was indeed detected for a few stars, these observations only covered the wavelength range 0.37–0.51 μm. The first observations to span and locate the peak of the polarization curve were made by Gehrels (1960).

When observed over the range of the optical and near-infrared (NIR) spectrum, interstellar polarization takes on a characteristic wavelength dependence, which can be parameterized through the relation

$$p(\lambda)/p_{\max} = \exp\left[-K \ln^2(\lambda_{\max}/\lambda)\right], \quad (2)$$

usually referred to as the Serkowski relation (Serkowski 1973), if K is set to the fixed value 1.15, or the Wilking relation (Wilking et al. 1980), if K is used as a fitting parameter. Codina-Landaberry & Magalhaes (1976) first suggested that K should be related to the size of the dust grains, and results from Wilking et al. (1982) and Whittet (1992) indicate that K and $\lambda_{\max}$ are likely correlated and thus not independent parameters. (See Whittet [1992] for an excellent review of the development of this parameterization.)

As has been shown by Kim & Martin (1994, 1995), the shape and variability of the polarization curve can be understood in terms of the size distribution of aligned grains, and thus $\lambda_{\max}$ provides a measure of the average size of the aligned grains. As noted by Kim & Martin (1995), only a very small fraction of the grains are likely to be aligned, and hence a degeneracy exists when using $\lambda_{\max}$ as a probe of grain alignment between the total grain size distribution and the fractional alignment in each size bin. This degeneracy is evident from the observational correlation of $\lambda_{\max}$ with R_V, the ratio of total to selective extinction, first noted by Serkowski (1968) (cf. Serkowski et al. 1975; Whittet & van Breda 1978), and is to be expected since, as shown by Kim et al. (1994), R_V traces the size distribution of the total grain population. As has been shown by, e.g., Vrba & Rydgren (1984), Vrba et al. (1993), and Whittet et al. (2001), R_V is in turn, in general, correlated with the visual extinction, A_V. This is usually interpreted as being due to grain coagulation causing the average grain size to increase at larger depths into the cloud (Bernard et al. 1993; Whittet et al. 2001; Wurm & Schnaiter 2002).

To break these degeneracies, it is important to measure each parameter to high precision and to seek out regions where the grain size distribution and alignment conditions vary over relatively small scales. The latter should, particularly if radiative processes drive the alignment, most likely be found in the outer parts of the clouds where the radiation field seen by the grains varies relatively rapidly. For the former, we need regions where sight lines at similar observed visual extinctions show significant differences in the grain size distributions.

A further complication in studying the variation of polarization is introduced by possible changes in strength or orientation of the magnetic field. To mitigate this concern, it is important to use line-of-sight samples reliably constrained to probe a single cloud.

While the visual extinction is a convenient and straightforward probe of the amount of material along the line of sight, it is important to remember that the line-of-sight extinction may not be a good probe of the relative radiation field seen by the material being probed, particularly at modest values of A_V. The three-dimensional geometry of the interstellar cloud, its relation to surrounding clouds and stars, and possible clumpiness of the material can cause the line-of-sight extinction to either over- or underestimate the "effective extinction," here defined as the minimum opacity, vis-à-vis the diffuse interstellar radiation field (ISRF), experienced by the material on the line of sight. As seen below, this is an important consideration in interpreting optical polarimetry.

The Southern Coalsack is a good target for studying the wavelength dependence of interstellar polarization and other absorption-based probes. The cloud is isolated and is well located in three dimensions. Its location, straddling the Galactic midplane, also guarantees a large number of background sources, whether hot stars are required or not. As shown by Andersson et al. (2004), the outer parts of the cloud show a wide range of values of R_V. We have argued that this likely reflects clumpy dust destruction in the cloud envelope caused by the hot gas in the Upper Centaurus-Lupus superbubble that envelopes the cloud. However, as we discuss below, for emission tracers, and in particular continuum emission, the location of the Coalsack in the Galactic plane can be a major disadvantage, since foreground and background emission may be difficult, or impossible, to tell apart.

For the purpose of the current study the important diffuse emission is the far-infrared (FIR) light attributable to dust grains heated by the ISRF. Several authors have used color temperatures based on the *IRAS* 60 μm–to–100 μm ratio to show that observationally this ratio provides a tracer of the radiation field impinging on the dust clouds (e.g., B5, Langer et al. 1989; B18 and Heiles Cloud 2, Snell et al. 1989; Ophiuchus, Jarrett et al. 1989). While it is likely that the analyses in these studies are only qualitatively valid due to the admixture of "large" and very small grains and might not provide accurate absolute temperatures, the usage of the 60 μm–to–100 μm ratio to trace the damping of the ISRF at different depths of a cloud is not in serious doubt (see, e.g., Draine & Li 2007). In the Appendix we use data from the clouds under study here to further support this usage.

For those areas and lines of sight where the interstellar extinction is dominated by a single cloud or cloud complex (such as on high Galactic latitude sight lines) we can be relatively sure that the visual extinction and FIR emission are both caused by the same material. However, for low Galactic latitude clouds, where background emission is significant, and clouds with significant (high mass) star formation, where the internally generated radiation field is comparable to the ISRF, the correlation of the visual extinction and FIR emission can be expected to break down.

In this study we have therefore complemented new multiband polarimetry of the Coalsack with archival polarimetry and other supporting data for five additional nearby interstellar clouds, Chamaeleon I (henceforth Chamaeleon), Musca, ρ Ophiuchus (henceforth Ophiuchus), R Corona Australis (henceforth R CrA), and Taurus, to address the alignment mechanism of interstellar grains.

The remainder of this paper is organized as follows. First, we present our new observations of the Southern Coalsack. In § 3.1 we present and discuss the analysis of the polarimetry for both the new Coalsack data and the reanalysis of the polarization

TABLE 1
Coalsack Target Stars

Star	Spectral Class[a]	V (mag)	$B-V$ (mag)	$(B-V)_0$ (mag)	$V-K$ (mag)	$(V-K)_0$ (mag)	R_V	A_V (mag)	References[b]	Screen?[c]
HD 108417	A1 V (1)	9.97±0.02	0.17±0.02	0.02±0.04	0.58±0.03	0.07±0.07	3.7±1.2	0.6±0.1	MSS	s
HD 108639	B1 III (2)	7.83±0.01	0.04±0.01	−0.27±0.06	...	−0.74±0.15	3.5±0.9	1.1±0.2	S89	...
CPD −64 1950	A8 (2)	9.64±0.03	0.61±0.03	0.52±0.08	1.72±0.04	1.35±0.06	4.5±4.3	0.4±0.1	S89	s
HD 108939	B8 III (2)	8.06±0.01	0.00±0.01	−0.11±0.09	0.17±0.02	−0.24±0.2	4.0±3.7	0.5±0.2	MSS	s
HD 109065	A1 V (2)	8.15±0.01	0.15±0.01	0.02±0.08	0.54±0.03	0.07±0.14	4.1±2.9	0.5±0.2	MSS	...
HD 110245	F8/G0 III (3)	8.39±0.01	0.68±0.01	0.55±0.10	2.28±0.03	1.75±0.25	4.3±3.9	0.6±0.3	MSS	...
HD 110432	B2 (2)	5.317±0.003	0.19±0.01	−0.24±0.06	1.36±0.05	−0.66±0.16	5.2±0.9	2.2±0.2	HGS69	...
HD 112045	A1 IV/V (2)	9.84±0.03	0.37±0.04	0.02±0.08	1.47±0.04	0.07±0.14	4.3±1.2	1.5±0.2	MSS	...
HD 112661	B0/1 III/IV (3)	9.26±0.02	0.55±0.02	−0.24±0.1	1.94±0.03	−0.78±0.2	3.8±0.6	3.0±0.2	MSS	s
HD 112954	B9 IV (1)	8.42±0.01	0.46±0.02	−0.06±0.06	1.56±0.03	−0.13±0.1	3.6±0.6	1.8±0.1	MSS	...
HD 112999	B6 III (1)	7.38±0.01	0.04±0.01	−0.15±0.02	0.26±0.02	−0.36±0.09	3.7±0.7	0.7±0.1	MSS	s
HD 113034	B0/1 III (3)	9.32±0.02	0.90±0.03	−0.24±0.1	3.16±0.03	−0.62±0.2	3.6±0.4	4.2±0.2	MSS	s
HD 114012	A0 V (1)	9.10±0.02	0.48±0.02	−0.02±0.04	1.35±0.03	0.00±0.07	2.9±0.3	1.5±0.1	MSS	...
HD 114720	B8 V (2)	9.65±0.03	0.07±0.03	−0.11±0.04	0.86±0.04	−0.24±0.2	6.6±2.2	1.2±0.2	MSS	...
HD 117111	B2V (1)	7.72±0.01	0.04±0.01	−0.24±0.02	0.71±0.04	−0.66±0.09	5.4±0.6	1.5±0.1	MSS	...

[a] Estimated uncertainties, in subclasses, are given in parentheses.
[b] Spectral classes from sources as defined below.
[c] Sight lines that are screened out in the *Hipparcos* field star–based analysis (see § 4.2).
References.—(HGS69) Hiltner et al. 1969; (MSS) Houk & Cowley 1975; (S89) Seidensticker & Schmidt-Kaler 1989.

data for the other five clouds, as well as supporting data consisting of optical, NIR, and FIR photometry. We show that the wavelength of maximum polarization is correlated with the visual extinction, albeit with many outliers. Section 3.2 proposes that the outliers in both the FIR and polarimetry data are due to cloud geometry and/or the presence of embedded (or nearby) stars, making the observed visual extinction a poor tracer of the radiation field seen by the dust. Section 3.3 shows that the FIR emission is anticorrelated with the visual extinction and that most of the outliers in the polarization plots can indeed be identified as outliers also in the FIR plots. This is expanded on in the Appendix. We then use the $I(60\ \mu\mathrm{m})/I(100\ \mu\mathrm{m})$ versus A_V relations to identify those sight lines where this is the case. Section 4.2 reanalyzes the $\lambda_{\max}$ versus A_V relations for the different clouds after the screening performed in § 3.3, and we find that there are now tight correlations for four of the six clouds. No such correlations are seen for $\lambda_{\max}$ versus R_V. However, the y-axis intercept for $\lambda_{\max}$ at $A_V = 0$ is correlated with $\langle R_V \rangle$. Section 4.3 discusses the dispersion seen in the $\lambda_{\max}$ versus A_V relation in terms of the characteristics of the embedded young stellar objects (YSOs) in the clouds.

2. OBSERVATIONS AND DATA REDUCTION

We used the University of Cape Town Polarimeter (UCTP; Cropper 1985) on the 1.9 m telescopes of the South African Astronomical Observatory (SAAO) during 2005 April 6–8 and 13 to perform multiband observations of interstellar polarization of stars background to the Southern Coalsack. The UCTP was configured in the simultaneous linear and circular polarimetry mode, with an RCA31034A GaAs photomultiplier as the detector. Measurements were performed using *UBVRI* filters in the Kron-Cousins system. We used HD 94851 and HD 98161 (Turnshek et al. 1990) as unpolarized standard stars and HD 155197, HD 154445 (Schmidt et al. 1992), and HD 93632 (Marraco et al. 1993) as polarized standard stars. At least one star from each class was observed each night. Measurements of the sky polarizations were acquired for each star immediately prior to and following the main observation. The data were reduced using a custom software package (Cropper 1985). None of the stars showed a statistically significant circular polarization in any band. Target star information is given in Table 1. Calibrated polarization for the Coalsack targets is summarized in Table 2.

3. ANALYSIS

3.1. *Polarization and Spectrophotometric Data*

For each target in our sample we fitted the polarization data with both the Serkowski and Wilking relations. We then performed an F-test (Lupton 1993) to determine whether the additional parameter associated with the "Wilking" equation was justified. Only for those data sets where the additional parameter was justified at the 90% level did we accept it. For those stars where it was not statistically justified we have left the column for "K" blank in the result tables. The parameter uncertainties were calculated by the fitting routines and verified using Monte Carlo simulations of the fits (Press et al. 1986, p. 529). Importantly for the present study, the wavelength of maximum polarization was rarely affected beyond the 1 σ level by the assumed or fitted value of K. This was also the case if we used, instead of a fixed K-value of 1.15, the relation $K = 1.66\lambda_{\max} + 0.01$ (Whittet 1992).

For all stars, the extinction parameters were recalculated and verified. Visual photometry was, where available, extracted from the Tycho database (Høg et al. 2000), while NIR photometry was extracted from the Two Micron All Sky Survey (2MASS), except where explicitly noted. Spectral classification was checked and updated. Intrinsic colors were estimated from Cox (2000), with uncertainties based on the reported uncertainties in the sources of the spectral classification and, where required, linear interpolation between the table entries.

3.1.1. *Coalsack Data*

Table 3 lists the best-fit parameters for the polarization curve fits for the Coalsack stars. Since we do not have any NIR polarimetry for the Coalsack stars, special care is needed to potentially justify the use of Wilking fits. For these stars we show the reduced χ^2 for the fits. We note that while the F-test justifies the additional free parameter of the Wilking fit for several stars,

TABLE 2

COALSACK POLARIMETRY RESULTS

Star	p_U (%)	θ_U (deg east of north)	p_B (%)	θ_B (deg east of north)	p_V (%)	θ_V (deg east of north)	p_R (%)	θ_R (deg east of north)	p_I (%)	θ_I (deg east of north)
HD 108417	0.49±0.05	78.7±1.4	0.59±0.03	78.1±0.9	0.64±0.03	78.1±0.7	0.64±0.03	72.7±0.7	0.69±0.03	76.1±0.8
HD 108639	1.69±0.04	88.5±1.3	1.85±0.03	90.5±0.9	1.91±0.03	90.1±0.8	1.84±0.03	88.6±0.8	1.65±0.03	88.7±1.0
CPD −64 1950	0.63±0.09	76.7±2.6	0.89±0.05	76.6±1.3	0.92±0.04	72.8±1.2	1.00±0.04	70.8±1.1	0.94±0.04	71.9±1.2
HD 108939	0.90±0.05	70.1±1.4	0.99±0.03	71.8±0.9	1.02±0.03	71.1±0.9	1.03±0.03	70.2±0.9	1.01±0.04	72.5±1.0
HD 109065	0.82±0.03	68.1±0.9	0.88±0.02	72.7±0.5	0.87±0.01	71.5±0.5	0.94±0.02	67.9±0.5	0.80±0.02	72.1±0.6
HD 110245	0.91±0.08	112.8±2.2	1.23±0.04	121.8±1.1	1.26±0.04	120.2±1.0	1.07±0.04	119.6±1.1	0.95±0.04	119.5±1.2
HD 110432	1.40±0.03	81.0±0.8	1.59±0.03	92.1±0.9	1.70±0.03	82.6±0.9	1.73±0.03	77.3±1.0	1.66±0.03	77.2±0.9
HD 112045	1.46±0.11	66.9±3.1	1.86±0.05	69.1±1.5	1.82±0.04	68.0±1.2	1.87±0.04	66.8±1.2	1.73±0.04	68.3±1.1
HD 112661	1.49±0.08	72.4±2.2	1.80±0.04	73.7±1.1	1.86±0.04	73.0±1.0	1.90±0.03	70.3±0.9	1.71±0.03	71.4±0.9
HD 112954	2.07±0.06	41.7±1.7	2.37±0.04	42.2±1.0	2.42±0.03	40.8±0.9	2.51±0.03	40.2±0.8	2.29±0.03	40.2±0.9
HD 112999	1.66±0.04	68.8±1.2	1.90±0.03	69.8±0.7	1.99±0.02	71.1±0.7	1.95±0.02	70.1±0.6	1.80±0.03	70.6±0.8
HD 113034	4.03±0.11	80.0±3.0	4.64±0.05	80.8±1.3	5.05±0.04	81.7±1.0	4.97±0.03	81.8±0.8	4.49±0.03	82.7±0.7
HD 114012	1.05±0.16	53.8±4.7	1.32±0.07	56.4±2.0	1.41±0.05	53.0±1.5	1.53±0.05	49.1±1.3	1.20±0.05	54.0±1.5
HD 114720	0.83±0.08	77.7±2.1	0.88±0.04	83.3±1.2	0.97±0.04	85.5±1.2	0.92±0.04	79.2±1.2	0.80±0.05	86.3±1.3
HD 117111	1.28±0.03	76.2±0.9	1.18±0.03	77.8±0.9	1.40±0.03	77.1±0.8	1.40±0.03	71.5±0.8	1.38±0.03	75.5±0.8

TABLE 3
Coalsack Polarization Curve Fits

Star	p_{max} (%)	λ_{max} (μm)	K	χ^2/ν_S	χ^2/ν_W
HD 108417	0.68±0.02	0.64±0.03	...	1.3	...
HD 108639	1.91±0.02	0.52±0.01	0.87±0.13	0.7	0.1
CPD −64 1950	0.99±0.02	0.63±0.03	...	0.8	...
HD 108939	1.03±0.02	0.62±0.05	0.42±0.27	2.6	0.2
HD 109065	0.90±0.01	0.54±0.01	...	10.4	...
HD 110245	1.22±0.02	0.50±0.02	...	3.2	...
HD 110432	1.73±0.02	0.62±0.02	0.69±0.12	4.2	0.1
HD 112045	1.92±0.02	0.57±0.01	...	3.1	...
HD 112661	1.92±0.02	0.57±0.01	...	0.9	...
HD 112954	2.52±0.02	0.57±0.01	...	5.9	...
HD 112999	1.99±0.02	0.56±0.01	0.88±0.10	2.1	0.5
HD 113034	5.05±0.02	0.574±0.005	...	0.35	...
HD 114012	1.44±0.03	0.57±0.02	...	2.6	...
HD 114720	0.95±0.02	0.54±0.02	...	0.3	...
HD 117111	1.45±0.01	0.58±0.01	...	21.6	...

in most cases the reduced χ^2 for these fits are then less than unity. The data and best-fit polarization curves are shown in Figure 1.

For HD 110432, the 2MASS data are flagged as being of poor quality; we therefore used an average of the results from Whittet & van Breda (1980), Dachs & Wamsteker (1982), and Dachs et al. (1988) for this star. In Figure 2 we plot the location of the derived wavelength of maximum polarization (λ_{max}) as a function of visual extinction. As noted above, earlier studies of the dependence of λ_{max} on extinction parameters have found a relationship with the value of the ratio of total to selective extinction (R_V; e.g., Whittet & van Breda 1978). We do not find such a correlation for the Coalsack data. In Figure 2 we have color-coded the sight lines according to their R_V values. While the two sight lines above $A_V = 2.5$ show R_V consistent with the value found at large visual extinction in this cloud ($R_V \approx 3.25$), no systematic trends in R_V are evident at smaller A_V.

One possible caveat to the accuracy of the calculated R_V values comes from the fact that several of the target stars are listed in some spectral classifications as either emission-line stars or possible binaries. To evaluate the possible influence of these complications for the Coalsack sample, we used the $J - H$ versus $H - K$ diagram, plotted in Figure 3. Since the direction of the reddening vector in this color-color diagram varies between regions (e.g., Racca et al. 2002), we calculated the $H - K$ color excess that, for each target, gave the smallest offsets between measured colors and best-fit reddened colors, given the spectral classifications of the stars and direction of the reddening vector. We used $E_{J-H}/E_{H-K} \approx 1.57$ (Kenyon et al. 1998) and $E_{J-H}/E_{H-K} \approx 1.91$ (Naoi et al. 2006) as test cases. In Figure 4 we plot the $H - K$ color excess versus the derived visual extinction. The measured difference $(H - K) - (H - K)_0$ is plotted by crosses with error bars. Open symbols represent the color excesses calculated assuming $E_{J-H}/E_{H-K} \approx 1.57$, while filled diamonds represent the color excesses calculated assuming $E_{J-H}/E_{H-K} \approx 1.91$. Only for HD 112661 and HD 112045 are offsets of more than 2 σ seen between the measured and best-fit $H - K$ color excesses (2.1 and 2.2 σ, respectively, for $E_{J-H}/E_{H-K} \approx 1.91$). While both of these stars are listed in SIMBAD as multiple, neither shows an exceptional R_V value. Even if these sight lines are suppressed, no correlation between λ_{max} and R_V is seen.

3.1.2. *Chamaeleon, Musca, Ophiuchus, R CrA, and Taurus Cloud Data*

Figure 2 shows a tight correlation of λ_{max} with A_V over the limited range of $A_V \sim 1.0$–2.5 but with outliers at both smaller and larger values of A_V. A similar weak correlation was noted by Whittet et al. (2001) in their Taurus data, but with a more pronounced scatter. To investigate whether the outlier points in the Coalsack plot are truly outliers in a real correlation, or whether the perceived correlation is instead a statistical fluke, we searched the literature for high-quality, multiwavelength polarimetry in sight lines penetrating well-defined interstellar clouds.

We selected five additional well-studied clouds with high-quality published multiwavelength polarimetry. Polarimetry data were extracted from the studies for Chamaeleon (Whittet 1992; Covino et al. 1997), Musca (Arnal et al. 1993), Ophiuchus (Whittet 1992; Vrba et al. 1993), R CrA (Whittet 1992), and Taurus (Whittet 1992; Whittet et al. 2001). To ensure as uniform a data set as possible in terms of photometry and stellar characteristics, we extracted visual (B, V) and NIR data from the Tycho and 2MASS archives. We verified and, where possible, updated the spectral classification, and then we assigned intrinsic colors as for the Coalsack stars. The resultant stellar characteristics are listed in Table 4. In a couple of cases unphysical values of, in particular, R_V are encountered, likely indicating problems with the spectral classification. These sight lines were therefore excluded from the subsequent analysis. In Figure 5 we compare the values of R_V and A_V derived here with those extracted from the literature. For both parameters, good agreement is seen. We note that the R_V values quoted in Arnal et al. (1993) are based on polarimetry and not on photometry, and we have therefore not included them in these plots.

As for the Coalsack sight lines, we fitted Serkowski or Wilking functions to the polarization data but selected only those stars with polarization measurements in at least four filters (for this reason we also chose not to include the Chamaeleon data from Whittet et al. 1994). The polarization fit parameters are given in Table 5. In most cases the λ_{max} derived here agree with those in the original papers within 1 σ of the mutual uncertainties and in all but one case within 2 σ. The one exception is the sight line toward HD 107875 in Musca (star number 7 in the nomenclature of Arnal et al. 1993), where the original paper reports $\lambda_{max} = 0.641 \pm 0.009$ μm, while we find $\lambda_{max} = 0.49 \pm 0.01$ μm using their stated polarization curve parameterization. Given this discrepancy, we have excluded this sight line from the analysis.

Plotting λ_{max} versus A_V for all six clouds (Fig. 6), we see that, particularly for Chamaeleon, Musca, and Taurus, a very similar structure is evident as for the Coalsack with a main grouping of points lying along what seems like a linear correlation from $A_V \sim 1$ to $\sim$2.5 mag, but with outliers at both small and large A_V. A critical issue, then, is whether the points we have here designated "outliers" are indeed that in a statistical sense, or whether the suggested correlation of λ_{max} with A_V over approximately 1–3 mag of extinction is illusory.

As noted above, two independent ways exist for estimating the extinction for a given parcel of gas and dust. However, neither the directly measured visual extinction nor the color-temperature relation of the FIR emission from the heated grains is immune to biases. We next discuss how the combination of the two tracers of extinction can be used to mitigate biasing in the determination of the effective opacity.

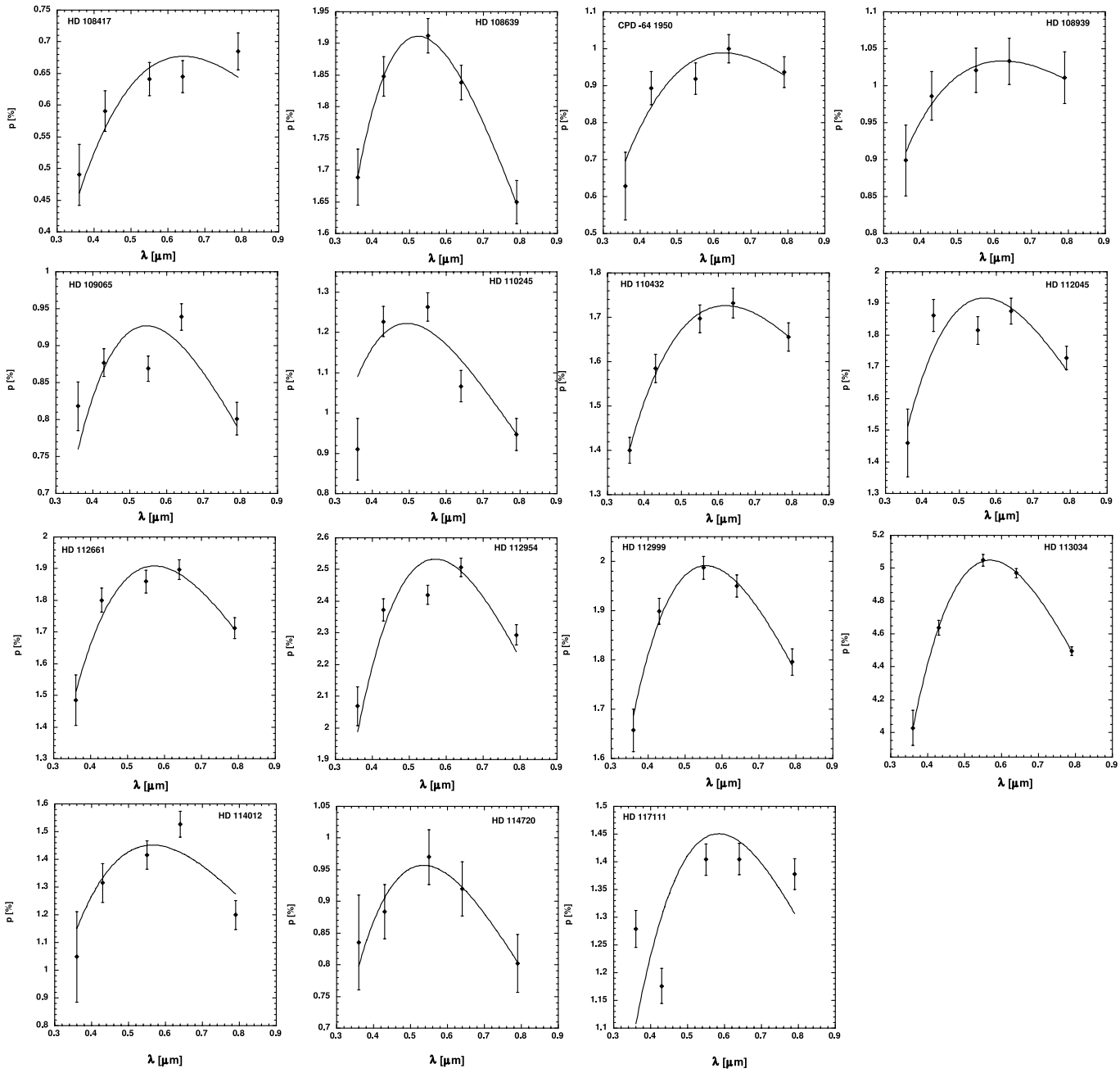

FIG. 1.—Measured multiband polarization for the Coalsack targets with best-fit polarization curve overlaid. Polarization fit parameters are listed in Table 3.

3.2. *Effective Extinction versus Line-of-Sight Extinction*

The line-of-sight extinction might not be a good indicator of the extinction (or, equivalently, radiation field) seen by the material sampled by an absorption (line or continuum) experiment—the effective extinction. Figure 7 illustrates some of the ways in which such discrepancies might occur. In this cartoon, we show a prolate cloud pointing toward the observer next to a roughly spherical cloud, with a "bridge" of material linking the two. The gray zone is meant to illustrate the part of the cloud into which the ISRF penetrates.

For sight line "A," which passes through the outskirts of the prolate cloud, the line-of-sight extinction is much larger than the effective extinction seen by the material probed. The average radiation field seen by different parcels along the chord is similar, and hence we would expect this kind of sight line to show a large A_V while retaining a relatively large 60 μm/100 μm ratio. A similar effect might arise if the sight line passes within the sphere of influence of an embedded, or nearby, stellar source contributing to the radiation field (A′).

For sight line "B" the line-of-sight extinction, again, is larger than that seen by the material, but here the different parcels along the chord see very different radiation fields. For this kind of sight line we would again expect a large A_V, but here, since the FIR radiation traces both radiatively heated dust and dust in the dark part of the cloud, we expect a low 60 μm/100 μm ratio.

For sight line "C," which passes through a region between clouds (or in an interclump region of a clumpy medium), the line-of-sight extinction instead underestimates the effective extinction

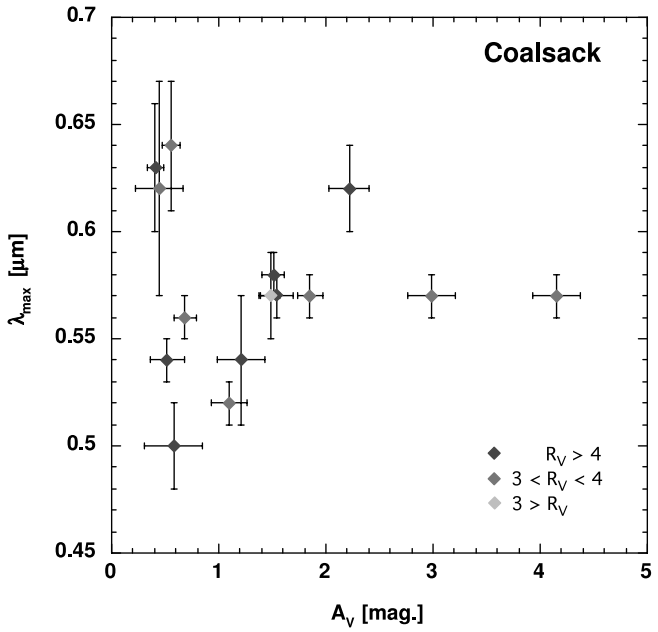

FIG. 2.—Wavelength of maximum polarization as a function of visual extinction for the newly observed stars behind the Southern Coalsack. The data points have been color-coded according to the measured values of the ratio of total to selective extinction along each line of sight. [*See the electronic edition of the Journal for a color version of this figure*.]

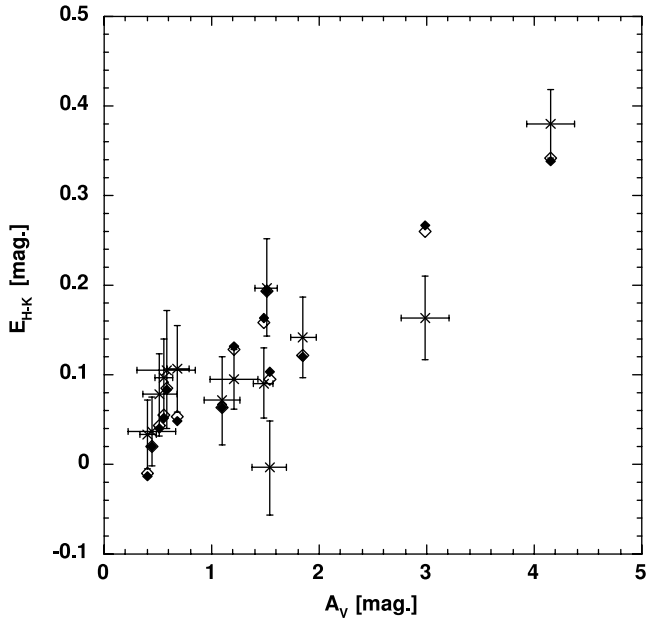

FIG. 4.—Measured $H - K$ color excess (*crosses*) together with the best-fit color excesses assuming two reddening laws from the literature. The largest offsets from the color excess for reddened intrinsic stellar colors are just above 2 σ and indicate at most minor contamination from circumstellar emission or binary companions.

experienced by the material due to shadowing effects by the surrounding clouds.

Finally, in sight line "D" the observed and effective extinctions are similar and the different parcels of material along the chord experience similar radiation fields.

Similar effects and observational discrepancies might also arise in a clumpy medium with the sight lines passing through predominantly clump or interclump material.

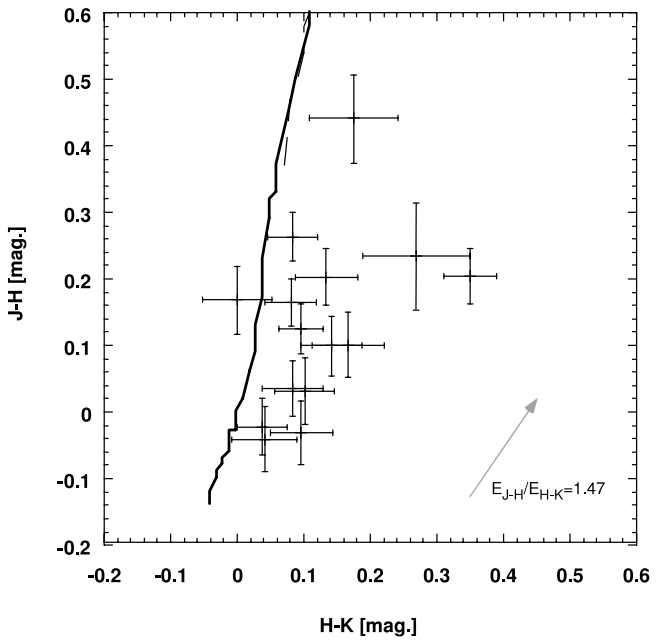

FIG. 3.—$J - H$ vs. $H - K$ color-color diagram for the Coalsack stars, showing a consistent reddening for all stars (except HD 113034) with a reddening slope around 1.5 (see text). The solid line shows the intrinsic colors of main-sequence stars, while the dashed line is for giants.

3.3. *Far-Infrared Data*

Empirically an anticorrelation is seen between column density and dust temperature based on the 60 μm–to–100 μm ratio in interstellar clouds (see, for instance, Fig. 8 of Snell et al. 1989). Since this ratio therefore indirectly traces the radiation field seen by the dust, we can use it as a probe of the effective extinction seen by the grain. While this emission is also likely prone to biases, such as variations in the fraction of small grains, we show in the Appendix that we can use the combination of visual extinction and FIR emission to screen the data sets for anomalous sight lines. We note that in this study we only do this in a relative sense for each cloud. We are not attempting to find absolute dust temperatures. While we limit our analysis to the 60 μm–to–100 μm ratio, we use the 25 μm–to–100 μm and 12 μm–to–100 μm ratios to argue in the Appendix that the local changes seen in the relation between the 60 μm–to–100 μm ratio and A_V are indeed likely due to irradiation differences.

We extracted FIR data from the IRIS rereduction (Miville-Deschênes & Lagache 2005) of the *IRAS* all-sky photometry. The spatial resolution of the IRIS maps is 3.8′, 3.8′, 4.0′, and 4.2′, respectively, for the 12, 25, 60, and 100 μm bands, but the maps are pixelized on a 1.5′ scale and hence oversampled by about a factor of 2.5–2.8. For the current study we used a 3×3 pixel average that allows us both to lessen the impact of any emission from the background star and to identify it, if significant. Comparing to the *IRAS* point (faint) source catalog, we find that, in most cases, the stars, when at all detectable, make only a minor contribution to the total FIR light on our lines of sight. This is especially true of the longer wavelength bands.

Since the nominal, single-pixel, photometric uncertainty in the IRIS maps is much smaller than the typical pixel-to-pixel variations (cf. Miville-Deschênes & Lagache 2005), we found that the standard deviation in the 3×3 pixel averages can be used as a sensitive indicator of stellar contamination of the FIR flux densities, complementing the *IRAS* point-source and faint-source catalogs. For those sight lines where the background star,

TABLE 4
STARS WITH DATA FROM ARCHIVES AND THE LITERATURE

Star	Spectral Class[a]	V (mag)	$B-V$ (mag)	$(B-V)_0$ (mag)	$V-K$ (mag)	$(V-K)_0$ (mag)	R_V	A_V (mag)	References[b]	Screen?[c]
					Chamaeleon					
F1	K4 III (2)	10.31±0.03	1.56±0.02	1.39±0.22	3.99±0.04	3.26±0.60	4.7±7.3	0.8±0.7	VR84	...
F2	B8 V (2)	9.90±0.03	0.51±0.03	−0.11±0.04	1.42±0.04	−0.24±0.12	3.0±0.3	1.8±0.1	VR84	...
F3	B4 V (1)	8.03±0.01	0.42±0.01	−0.19±0.02	1.65±0.02	−0.49±0.07	3.9±0.2	2.4±0.1	MSS	...
F6	A2 V (1)	10.85±0.08	0.74±0.11	0.05±0.03	1.63±0.08	0.14±0.07	2.4±0.4	1.6±0.1	VR84	s
F7	B5 V (2)	10.25±0.04	0.41±0.06	−0.17±0.04	1.15±0.05	−0.42±0.12	3.0±0.4	1.7±0.1	VR84	...

NOTES.—Table 4 is published in its entirety in the electronic edition of the *Astrophysical Journal*. A portion is shown here for guidance regarding its form and content.

[a] Estimated uncertainties, in subclasses, are given in parentheses.

[b] Spectral classes from sources as defined below.

[c] Sight lines that are screened out in the *Hipparcos* field star–based analysis (see § 4.2).

[d] The derived value is unphysical and is ignored in the following.

[e] Based on comparisons of Fig. 1 in Arnal et al. (1993) with the Aladin tool (Bonnarel et al. 2000), we have made the following target identifications in Musca from Arnal et al. (1993) (AMZ): AMZ16=CD −71 836; AMZ18=CD −71 832; AMZ28=CD −70 925; AMZ41=CPD −69 1677; AMZ45=CD −69 1024.

REFERENCES.—(KDH94) Kenyon et al. 1994; (M68) Metreveli 1968; (MSS) Houk & Cowley 1975; (N95) Nesterov et al. 1995; (SCH85) Straizys et al. 1985; (SM80) Straizys & Meistas 1980; (SSS80) Slutskij et al. 1980; (U85) Ungerer et al. 1985; (VR84) Vrba & Rydgren 1984; (VR85) Vrba & Rydgren 1985; (VR93) Vrba et al. 1993; (W01) Whittet et al. 2001; (W84) Whittet et al. 1987; (W87) Whittet et al. 1987; (Y) VizieR Online Data Catalog, 1141 (U. Yale, 1997).

or a nearby star, contributes to the average, the standard deviation increases dramatically compared to the norm.

3.3.1. *Nominal $I(60\ \mu\mathrm{m})/I(100\ \mu\mathrm{m})$ versus A_V Relations*

We can probe the difference between line-of-sight and effective extinction by comparing the observed visual extinction to the amount of emission due to heated grains, as probed by the ratio of 60 μm to 100 μm flux densities. To find a nominal relationship for each cloud, we used sight lines with reliably determined visual extinctions and compared these to the FIR data. We used two partially overlapping data sets for this analysis: Field stars were first selected from the *Hipparcos* catalog, providing trigonometric parallaxes and thus allowing a clean separation of the stars into groups foreground and background to the cloud, but with a fairly limited total number of sight lines. We also used the catalog of Tycho stars with known spectral classifications (Wright et al. 2003) to maximize the number of sight lines used. In this case, we usually do not have explicit distance information, and we therefore imposed somewhat more stringent selection criteria for which stars to include in the analysis.

For the first field star samples we selected all stars in the *Hipparcos* catalog within a 3° radius of $(l, b) = (297°, -15.5°)$, $(354°, 15°)$, $(0°, -19.5°)$, and $(174°, -14°)$ for the Chamaeleon, Ophiuchus, R CrA, and Taurus clouds, respectively. For the Musca cloud we used a 2° radius centered on $(l, b) = (301°, -8°)$. For the Coalsack, we used the target list of Seidensticker (1989) as input in our *Hipparcos* search. From these original lists we then selected stars at distances (based on the *Hipparcos* trigonometric parallaxes) greater than those estimated for the clouds. Complementing the Tycho photometry with 2MASS NIR photometry, we calculated visual extinctions. We rejected stars with negligible extinction and were left with samples of 39, 30, 23, 34, and 27 field stars for Chamaeleon, Musca, Taurus, R CrA, and Ophiuchus clouds, respectively.

For the second sample we selected stars as above from the catalog of Wright et al. (2003) for Chamaeleon, Coalsack, Musca, Ophiuchus, and R CrA. For Taurus, because of the elongated

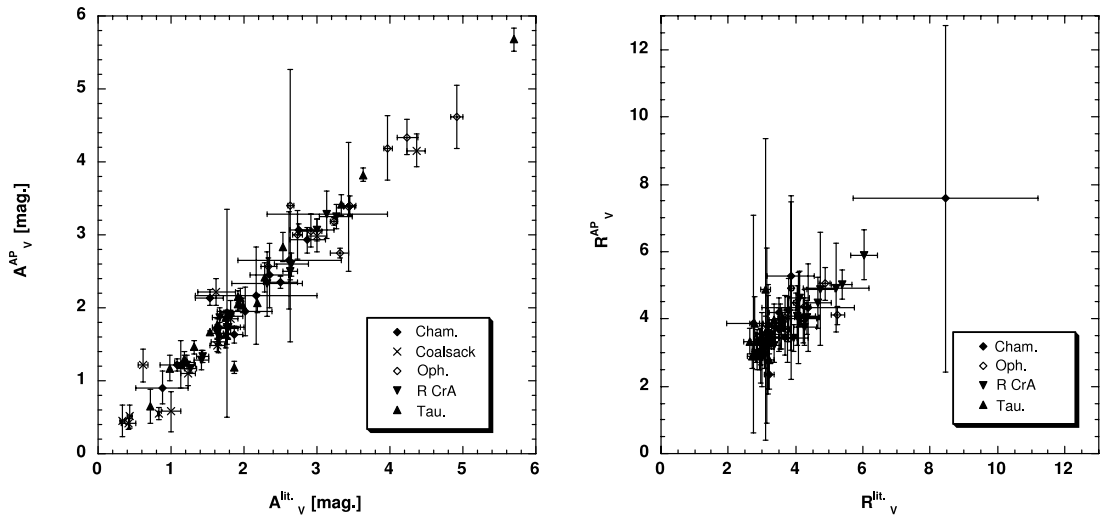

FIG. 5.—Values of A_V and R_V derived here compared with those extracted from the literature. Data for Chamaeleon are from Vrba & Rydgren (1984), for Ophiuchus from Vrba et al. (1993), for R CrA from Vrba & Rydgren (1984), and for Taurus from Whittet et al. (2001). Arnal et al. (1993) did not publish visual extinctions, and their quoted R_V values were calculated from $\lambda_{\max}$ fits; hence, Musca is not included here. Good agreement is seen for both parameters.

TABLE 5
Polarization Curve Fits for Stars from the Literature

Star	p_{max} (%)	λ_{max} (μm)	K
	Chamaeleon		
F1	3.35±0.04	0.547±0.007	0.82±0.05
F2	3.85±0.03	0.625±0.007	1.03±0.05
F3	5.45±0.04	0.655±0.005	...
F6	5.48±0.03	0.576±0.007	1.00±0.03
F7	5.92±0.02	0.538±0.005	0.82±0.01

Notes.—Table 5 is published in its entirety in the electronic edition of the *Astrophysical Journal*. A portion is shown here for guidance regarding its form and content.

shape of the cloud, we selected stars within a 3° radius of two centers at $(\alpha, \delta) = (04^h40^m00^s, 25°30'00'')$ and $(04^h15^m00^s, 28°00'00'')$. As with the *Hipparcos* sample, we extracted Tycho and 2MASS photometry and calculated visual extinctions and ratios of total to selective extinctions. Based on A_V versus distance diagrams from the *Hipparcos* samples, we then selected only those stars with $A_V > \{0.3, 0.4, 0.4, 0.4, 0.3, 0.5\}$ for Chamaeleon, Coalsack, Musca, Ophiuchus, R CrA, and Taurus, respectively. We used the *IRAS* point- and faint-source catalogs to screen out stars detected as point sources and finally screened for unreasonable values of R_V, which likely reflect unreliable spectral classifications. Finally, we eliminated small regions (usually 0.5° or 1° radii) around stars where the I_{60}/I_{100} ratio showed localized influence from those stars (see the Appendix). We were then left with 90, 231, 60, 58, 96, and 154 stars, respectively, for the six clouds.

Because of the relatively bright limiting magnitude of the *Hipparcos* database, the size of the area used to select the field stars involves a trade-off between the largest acceptable distance from the cloud center and number statistics. While the polarization samples do cover smaller areas on the sky, the 3° radius (2° for Musca) was chosen based on emission-line and extinction maps (e.g., Cambrésy 1999). Although we do not have kinematic data tracing the material giving rise to the extinction in the field star samples, we can use the measured A_V values to see that this sample likely does probe the outer layers of the molecular clouds under study. Our *Hipparcos* field star samples have visual extinctions of $A_V\{\text{min, max, mean}\} = \{0.3, 2.4, 1.0\}$ mag for Chamaeleon, $\{0.1, 2.4, 0.9\}$ mag for the Coalsack, $\{0.4, 1.7, 0.77\}$ mag for Musca, $\{0.4, 4.5, 1.6\}$ mag for Ophiuchus, $\{0.1, 1.7, 0.6\}$ mag for R CrA, and $\{0.4, 3.3, 1.3\}$ mag for Taurus. As shown by Savage et al. (1977) and Rachford et al.

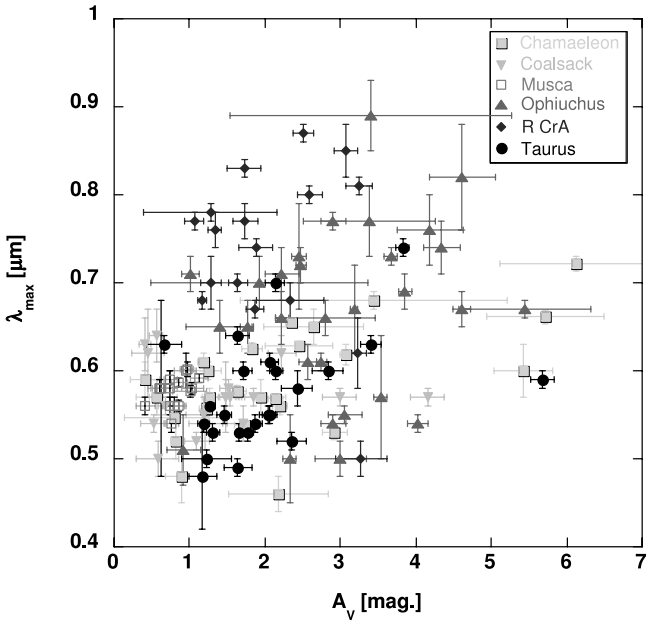

Fig. 6.—Wavelength of maximum polarization as a function of visual extinction for the sight lines through the Chamaeleon, Musca, Ophiuchus, R CrA, and Taurus clouds. For Chamaeleon, Musca, and Taurus a similar structure is seen in the distribution of points as that noted for the Coalsack. [*See the electronic edition of the Journal for a color version of this figure.*]

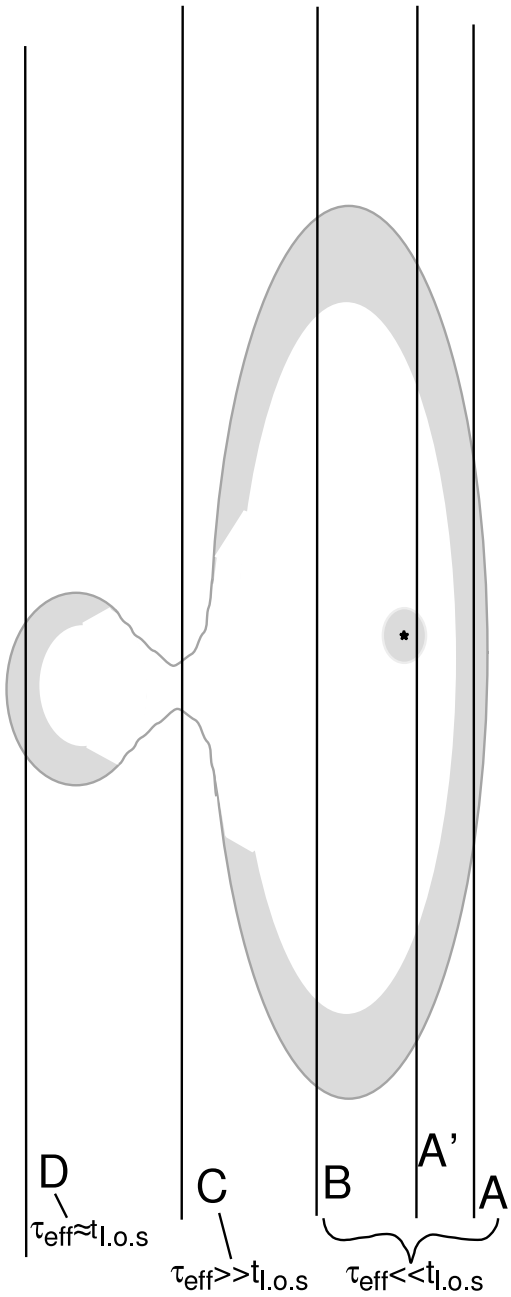

Fig. 7.—Possible origins of differences between line-of-sight extinction and effective extinction. For an asymmetrical cloud with its long axis close to the line of sight, the measured visual extinction, A_V, can both over- and underestimate the extinction experienced by the gas and dust on the line of sight. See text for details.

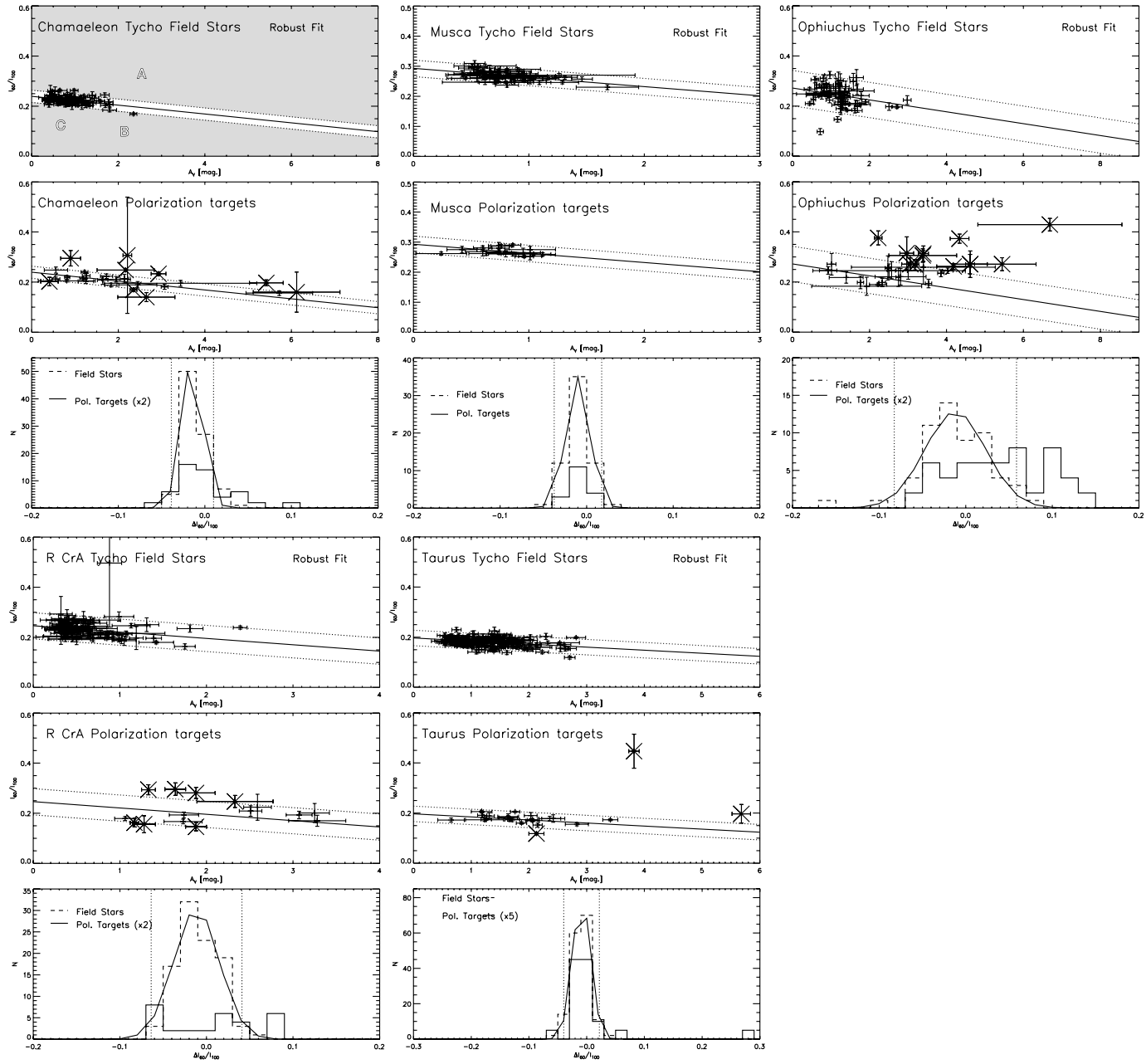

FIG. 8.—Anomalous sight lines are found comparing the I_{60}/I_{100} ratios to the measured visual extinction. The top panel for each cloud shows the relationship found between I_{60}/I_{100} ratios and A_V for the field star samples selected from the Wright et al. (2003) catalog. The middle panels overplot these best fits on the data for the polarization target samples. The bottom panels show the distribution of fit residuals for the field star samples (*dashed histograms*) and polarization target samples (*solid histograms*). Also plotted are the best-fit Gaussians for the field star samples (*solid line*) and the $\pm 2\ \sigma$ limits used for screening targets as anomalous (*dotted lines*). The shaded regions in the top panel for Chamaeleon illustrate the approximate areas corresponding to the "sight line types" discussed in the text and illustrated in Fig. 7. This "debiasing" technique fails for the Coalsack sight lines, presumably due to the strong FIR background in the Galactic plane. See text for details.

(2002), the transition to molecular hydrogen occurs already at $E_{B-V} \sim 0.1$ ($A_V \sim 0.3$), and hence most of our field star sight lines probe molecular material. In addition, as shown by, e.g., Wannier et al. (1983), van der Werf et al. (1989), and Andersson & Wannier (1993), molecular clouds are surrounded by extensive atomic envelopes. Figure 3 of Boulanger et al. (1998) also illustrates this for the Chamaeleon complex. Particularly for the high-latitude clouds in our study, it is thus unlikely that the field stars probe material unrelated to the clouds probed by the polarimetry.

As we are explicitly searching out, and expecting to find, points where the systematic errors dominate the random ones, we used a robust fitting algorithm (Press et al. 1986, p. 539) to find the nominal $I(60\ \mu\text{m})/I(100\ \mu\text{m})$ versus A_V relations for each cloud. This algorithm uses an iterative procedure based on Tukey's biweight weighting with a limit of 6 outlier-resistant standard deviations (Press et al. 1986), as implemented in the IDL routine `robust_linefit`, available in the `astron` library.[1]

[1] Available at http://idlastro.gsfc.nasa.gov.

For the larger Tycho sample we also used weighted linear fits. The two algorithms yield very similar fitting parameters in this case.

For the *Hipparcos* samples, the robust fits for Chamaeleon, Musca, Ophiuchus, R CrA, and Taurus yield

$$\frac{I_{60}}{I_{100}} = \begin{matrix}(0.241 \pm 0.005)\\ (0.29 \pm 0.01)\\ (0.27 \pm 0.02)\\ (0.21 \pm 0.01)\\ (0.196 \pm 0.008)\end{matrix} - A_V \times \begin{matrix}(0.022 \pm 0.005)\ [\mathrm{Cham}]\\ (0.026 \pm 0.010)\ [\mathrm{Musc}]\\ (0.01 \pm 0.02)\ [\mathrm{Oph}]\\ (0.035 \pm 0.01)\ [\mathrm{R\ CrA}]\\ (0.013 \pm 0.006)\ [\mathrm{Tau}]\end{matrix} . \quad (3)$$

For the Tycho samples, the robust fits yield

$$\frac{I_{60}}{I_{100}} = \begin{matrix}(0.240 \pm 0.004)\\ (0.29 \pm 0.1)\\ (0.27 \pm 0.1)\\ (0.244 \pm 0.006)\\ (0.179 \pm 0.003)\end{matrix} - A_V \times \begin{matrix}(0.018 \pm 0.004)\ [\mathrm{Cham}]\\ (0.030 \pm 0.007)\ [\mathrm{Musc}]\\ (0.024 \pm 0.010)\ [\mathrm{Oph}]\\ (0.023 \pm 0.007)\ [\mathrm{R\ CrA}]\\ (0.012 \pm 0.002)\ [\mathrm{Tau}]\end{matrix} . \quad (4)$$

In Figure 8 we show the best linear fits (*solid lines*, *top panels*) using the robust fitting algorithm to the Tycho field star samples only (i.e., the polarization targets were not included in the fits).

For Chamaeleon, Musca, Ophiuchus, R CrA, and Taurus well-defined linear correlations are found (for Ophiuchus, the uncertainties on the fit coefficients for the *Hipparcos* sample are too large for the fit to be significant). For the Coalsack, which straddles the Galactic plane, this technique fails to provide a reasonable correlation, presumably because of the strong influence of diffuse background sources in the FIR data.

The middle panels of Figure 8 show the locations of the polarization targets in the FIR versus A_V diagrams.

In the bottom panels of Figure 8 we show the distributions of offsets in I_{60}/I_{100} from each data point to the best-fit line at the same value of A_V (dashed histograms for the field stars and solid histograms for the polarization targets) and the best-fit Gaussians to these distributions. The widths of the distributions are similar for all clouds ($\sigma = 0.012$, 0.014, 0.036, 0.026, and 0.016, respectively). Based on similar geometrical arguments as for Figure 7, it is likely that these widths trace the porosity of the outer parts of the clouds where the radiative grain heating occurs. In the Appendix we show that the widths of these dispersions are correlated with the star formation rate (SFR) in the clouds.

The dashed lines in Figure 8 show the 2 σ distance from the best-fit solution. Points below and to the left of the left-hand dashed lines are likely to have characteristics of sight line "B" in Figure 7, for high values of A_V, or sight line "C," for low values of A_V, while points above and to the right of the right-hand dashed lines are likely to have characteristics of sight line "A."

We note that with the exception of the identified outliers, the polarization sample targets and the field stars overlap in the well-defined Gaussian distributions in offset from the fits, providing additional support for the assumption that the two observational samples are drawn from a common parent population.

While the above screening method fails for the Coalsack, inspecting the $\lambda_{\max}$ versus A_V plot for the Coalsack and comparing it to those of Chamaeleon and Taurus, we can see that the points at relatively high extinction and relatively low $\lambda_{\max}$ in the Coalsack have corresponding sight lines in both Chamaeleon and Taurus and that these sight lines in the Coalsack fall in the equivalent "A" region in the I_{60}/I_{100} versus A_V plot as their counterparts for Chamaeleon and Taurus. Similarly, the points at high $\lambda_{\max}$ and low A_V are similar to points in region "C" for Chamaeleon in both the $\lambda_{\max}$ versus A_V and I_{60}/I_{100} versus A_V plots. While based on a more indirect and less satisfactory procedure, we therefore screen these points also in the Coalsack sample. In Figure 9 we show the resulting I_{60}/I_{100} versus A_V plot with the sources thus deselected marked. The width of the $\Delta I_{60}/I_{100}$ distribution for the remaining sight lines for the Coalsack is $\sigma = 0.04$, also similar to the values found for the other clouds.

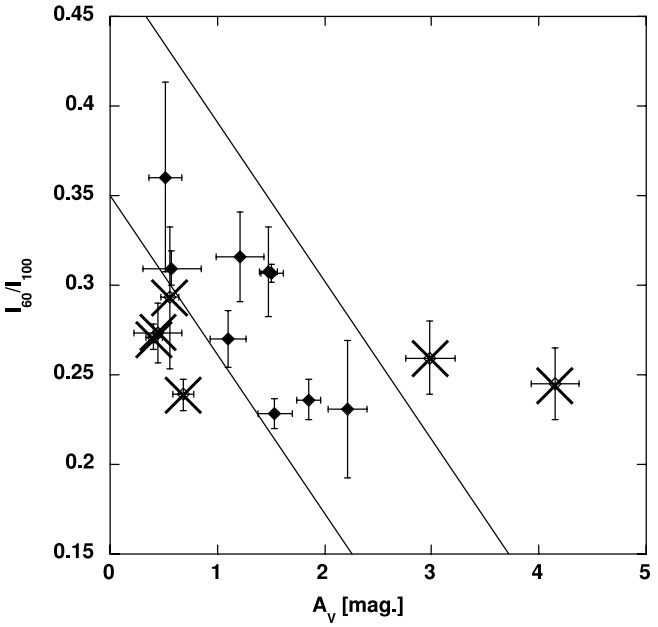

FIG. 9.—For the Coalsack, establishing a nominal A_V vs. I_{60}/I_{100} slope fails, presumably due to the influence of background emission in the *IRAS* data. We therefore screened the Coalsack data based on similarities with the Chamaeleon and Taurus plots. The screened-out sources are marked with crosses.

4. RESULTS AND DISCUSSION

4.1. *Origin of the Outliers*

We argue that the outliers in Figure 8 are likely primarily due to localized differences in the irradiation of the dust. The Appendix provides several direct lines of evidence in favor of this interpretation. For Chamaeleon and R CrA all the sight lines identified as type "A" can be seen to be due to proximity to HD 97300 or HD 175362, respectively. Similarly, for Ophiuchus almost all type "A" sight lines can be seen to be close to either σ Sco or ρ Oph D (Fig. 10). In addition, as also shown in the Appendix, the ratio I_{60}/I_{100} shows a stronger response to the vicinity of a hot star than I_{25}/I_{100}, while the I_{12}/I_{100} ratio shows little or no response to the proximity of hot stars. These results provide strong support for an origin in irradiation differences. As shown in the Appendix, the dispersion around the best-fit lines in the I_{60}/I_{100} versus A_V plots is correlated with the characteristics of the star formation in the cloud (see below). We interpret this as due to increasing porosity (clumpiness) in the clouds produced by increasing star formation activity, which

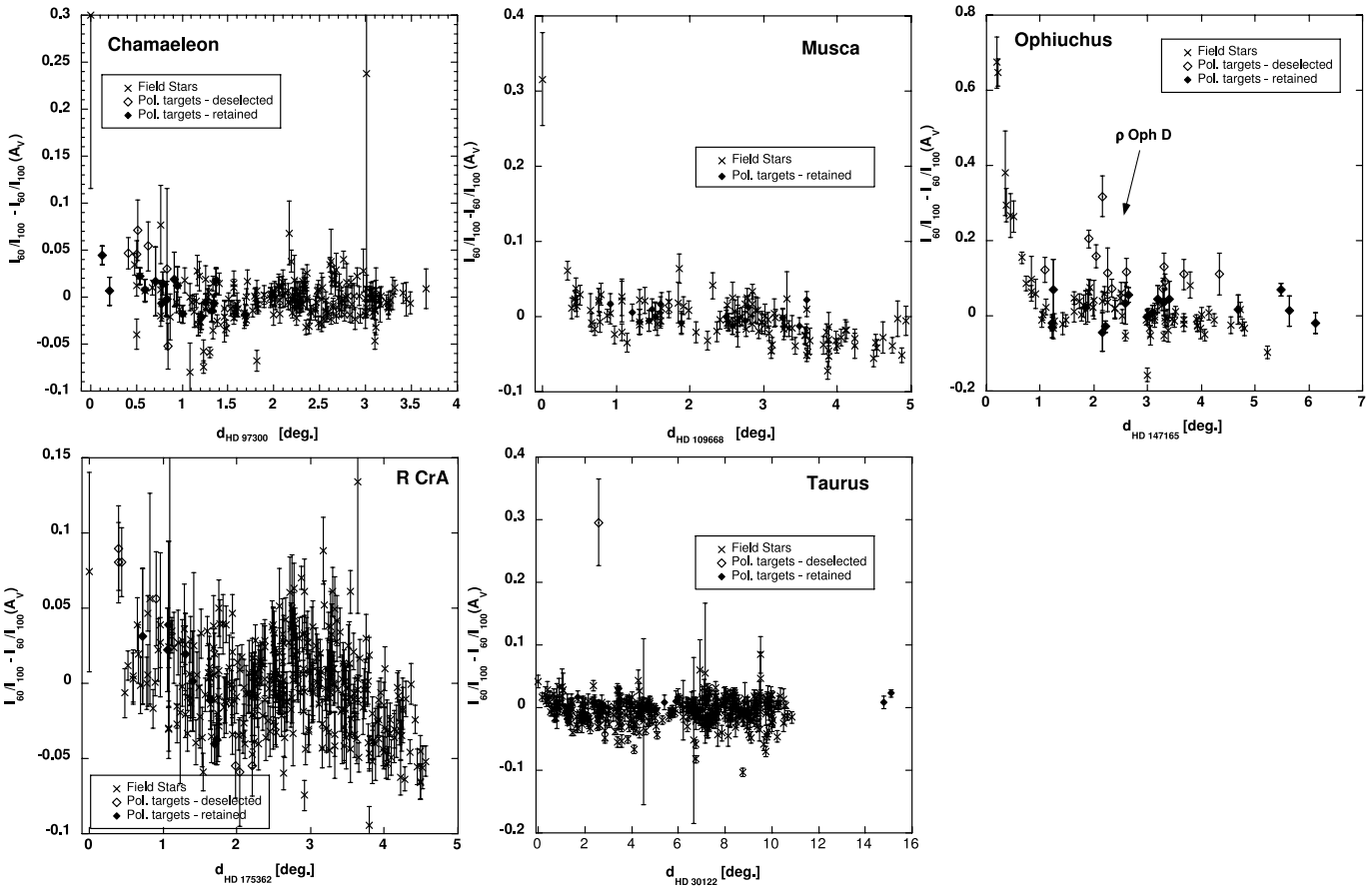

FIG. 10.—Offset from the best-fit I_{60}/I_{100} vs. A_V relations (Tycho-selected field stars) plotted as functions of the two-dimensional distance from nearby hot stars. For lines of sight through Chamaeleon the dominant star is HD 97300 (*top left panel*); for Musca, HD 109668; for Ophiuchus, σ Sco and ρ Oph D both yield noticeable effects. For lines of sight through R CrA and Taurus the dominant stars are HD 175362 and HD 30122, respectively. Stars from the Tycho field star samples are plotted with crosses, while diamonds indicate stars in our polarization samples. Open diamonds indicate sight lines classified as "anomalous." The polarization sample stars with the largest offsets tend to be located close to the hot stars, indicating that many of the anomalous I_{60}/I_{100} ratios are due to the additional irradiation from these stars.

changes the radiative transfer of the light heating the dust grains. A quantitative analysis of this clumpy transfer is beyond the scope of the present paper.

It should be noted that the screening procedure used in Figure 8 does not rely on this interpretation. The screening as such is a straightforward numerical procedure and uses an explicit numerical limit for which sight lines to label "anomalous." The use of the $I(60\ \mu\text{m})/I(100\ \mu\text{m})$ versus A_V ratio to screen the polarimetry data should also not introduce any biases in the latter. This is because only a very small fraction of the grains contribute to the polarization (Kim & Martin 1995), while all grains contribute to the FIR emission. Also, even if the outliers in Figure 8 were due to significant enhancements in the population of very small grains (VSGs), the size distributions of the VSGs and the grains responsible for the visual polarization have, at most, a minute overlap (Kim & Martin 1995; Desert et al. 1990).

4.2. *Debiased $\lambda_{\max}$ versus A_V Plots*

In Figures 11 and 12 we show the plots of $\lambda_{\max}$ versus A_V that result if we reject the points in Figure 8 that fall more than 2 σ from the robust fits for the Tycho sample. Overlaid are the best linear fits for each cloud (*solid lines*). The dashed lines represent the relations based on the average slope from all the clouds and a zero intercept based on the mean value of R_V of the cloud (see below). Very similar plots result for the *Hipparcos*-based screening, with the main difference that the R CrA sample shows a broader scatter. We show the $\lambda_{\max}$ versus A_V plot for R CrA using the *Hipparcos* screening in Figure 13. In what follows, except were explicitly noted, we discuss these "debiased" data sets.

Three conclusions can immediately be drawn from these new plots:

1. While the plot of $\lambda_{\max}$ versus A_V including all the data shows only a very weak correlation, the "screened" plot shows a distinct correlation of $\lambda_{\max}$ with A_V for Chamaeleon, Coalsack, Musca, and Taurus and consistent results for Ophiuchus and R CrA. We can quantify the latter statement by performing Spearman rank-order tests on the two groups of data sets. For Chamaeleon and Taurus both the unscreened and *Hipparcos* screened data sets show small (<6%) probabilities for being uncorrelated (the Tycho screened sets yield 2% and 14% probabilities). For the Coalsack the probability for an accidental correlation drops from 44% to 6% after screening. For Musca (where no sight lines are screened) we find an 18% probability of being uncorrelated.

2. Within each individual cloud sample, no obvious correlations are seen between $\lambda_{\max}$ and R_V.

3. It now is clear to the eye that the slopes of $\lambda_{\max}$ versus A_V in the individual clouds are very similar, but the three groups are

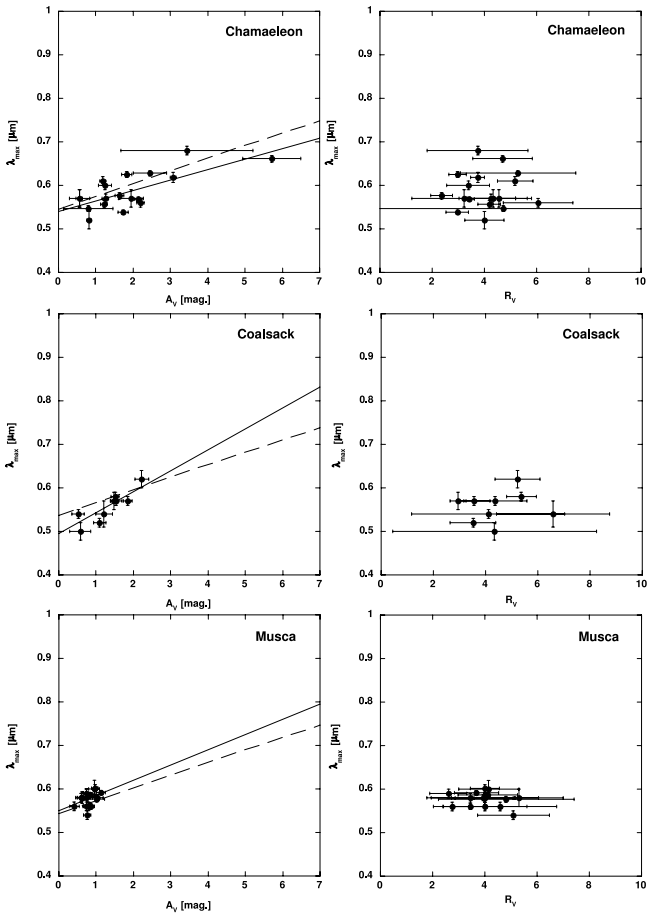

FIG. 11.—Plots of $\lambda_{\max}$ vs. A_V for the debiased sample for Chamaeleon, Coalsack, and Musca. For each cloud, the best fit (using a robust linear fit) is overplotted as a solid line. The dashed lines represent the "universal slope" of 0.028 and zero intercepts determined from the average R_V for the cloud. The *Hipparcos* screened sample yields similar plots.

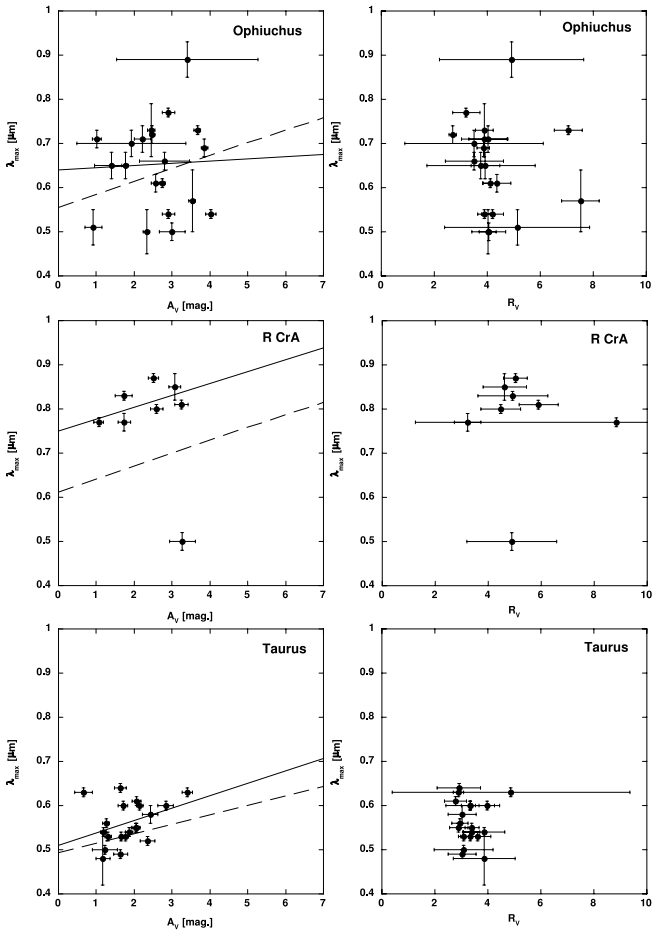

FIG. 12.—Same as Fig. 11, but for Ophiuchus, R CrA, and Taurus. For Ophiuchus and Taurus the *Hipparcos* screened samples yield similar plots. For R CrA a significantly different selection is encountered, which is illustrated in Fig. 13.

offset from each other in $\lambda_{\max}$. We used robust fits to quantify this and find that for the *Hipparcos* screened sample

$$\lambda_{\max} = \begin{matrix}(0.54 \pm 0.02)\\(0.50 \pm 0.02)\\(0.55 \pm 0.02)\\(0.60 \pm 0.05)\\(0.72 \pm 0.10)\\(0.48 \pm 0.02)\end{matrix} + A_V \times \begin{matrix}(0.04 \pm 0.01)\ \text{[Cham]}\\(0.05 \pm 0.01)\ \text{[CS]}\\(0.04 \pm 0.02)\ \text{[Musc]}\\(0.01 \pm 0.03)\ \text{[Oph]}\\(0.01 \pm 0.08)\ \text{[R CrA]}\\(0.05 \pm 0.01)\ \text{[Tau]}\end{matrix}, \quad (5)$$

while for the Tycho screened sample

$$\lambda_{\max} = \begin{matrix}(0.54 \pm 0.01)\\(0.50 \pm 0.02)\\(0.55 \pm 0.02)\\(0.64 \pm 0.05)\\(0.75 \pm 0.03)\\(0.51 \pm 0.02)\end{matrix} + A_V \times \begin{matrix}(0.024 \pm 0.006)\ \text{[Cham]}\\(0.05 \pm 0.01)\ \text{[CS]}\\(0.04 \pm 0.02)\ \text{[Musc]}\\(0.01 \pm 0.03)\ \text{[Oph]}\\(0.03 \pm 0.02)\ \text{[R CrA]}\\(0.03 \pm 0.02)\ \text{[Tau]}\end{matrix}. \quad (6)$$

The slopes in $\lambda_{\max}$ versus A_V are all very close and, in particular, those for Chamaeleon, Coalsack, Musca, and Taurus are all

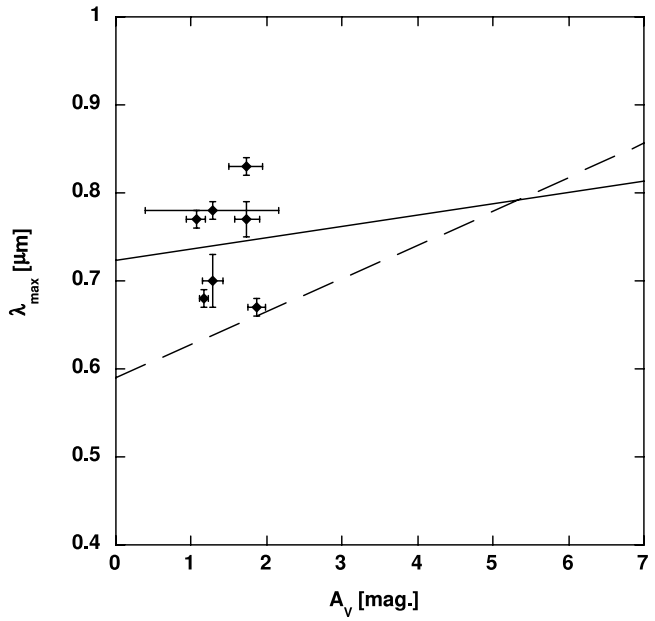

FIG. 13.—Plot of $\lambda_{\max}$ vs. A_V for the debiased R CrA sample screened based on the *Hipparcos* field stars. As in Fig. 11, the best fit (using a robust linear fit) is overplotted as a solid line. The dashed line represents the universal slope of 0.038 and zero intercept determined from the average R_V for the cloud.

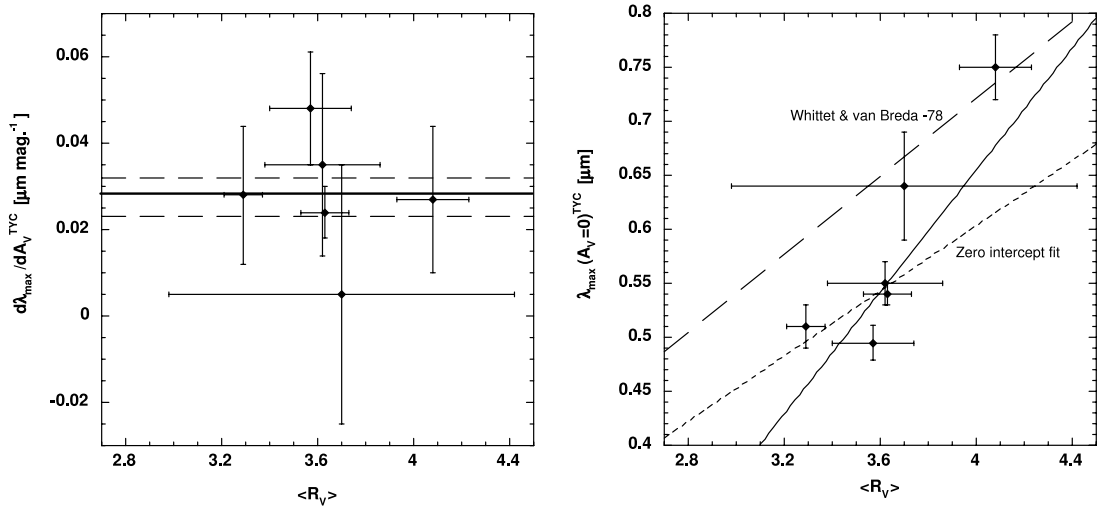

FIG. 14.—Slope (*left*) and zero intercepts of the $\lambda_{\max}$ vs. A_V (*right*) for the six clouds under study compared to the average of the ratio of total to selective extinction, using the Tycho screened samples. The solid and dashed lines in the left panel illustrate the weighted average of the slope and its uncertainty. The solid line in the right panel shows the best fit for $\lambda_{\max}$ vs. A_V, allowing a nonzero intercept. The short-dashed line shows the best fit assuming a zero intercept. The long-dashed line corresponds to the R_V vs. $\lambda_{\max}$ correlation found by Whittet & van Breda (1978).

very close and have small error bars, indicating that the slope is universal (Figure 14, *left panel*). A weighted average of the slopes yields $d\lambda_{\max}/dA_V = 0.028 \pm 0.005$ (0.038 ± 0.007) for the Tycho (*Hipparcos*) screened samples.

As has been shown by Whittet & van Breda (1978), $\lambda_{\max}$ is generally found to be correlated with R_V. This is not surprising since, as has been shown by Kim & Martin (1994, 1995), changes in both $\lambda_{\max}$ and R_V are most sensitive to changes in the population (total and aligned part) of the smaller grains. In the right panels of Figure 11 we plot $\lambda_{\max}$ versus R_V for the screened samples. No correlations are seen even for the clouds where correlation in the $\lambda_{\max}$ versus A_V plots is evident.

We calculated weighted averages of R_V for the full polarization target samples and find $R_V = 3.6 \pm 0.1$, 3.6 ± 0.2, 3.6 ± 0.2, 3.7 ± 0.7, 4.1 ± 0.2, and 3.3 ± 0.1 for Chamaeleon, the Coalsack, Musca, R CrA, and Taurus, respectively. In Figure 14 (*right panel*) we plot the result with the best linear fit of the zero intercept of $\lambda_{\max}$ [$\lambda_{\max}(A_V = 0)$] for the Tycho screened samples with the average R_V. The best, weighted fit yields

$$\lambda_{\max}(A_V = 0) = (-0.47 \pm 0.16) + (0.28 \pm 0.04)\langle R_V \rangle, \quad (7)$$

or, if we impose a zero intercept,

$$\lambda_{\max}(A_V = 0) = (0.151 \pm 0.002)\langle R_V \rangle. \quad (8)$$

For the *Hipparcos* screened sample the equivalent fits yield

$$\lambda_{\max}(A_V = 0) = (-0.26 \pm 0.24) + (0.22 \pm 0.07)\langle R_V \rangle, \quad (9)$$

or, if we impose a zero intercept,

$$\lambda_{\max}(A_V = 0) = (0.146 \pm 0.002)\langle R_V \rangle. \quad (10)$$

In both cases the zero-intercept fit is close to the $\lambda_{\max} = (0.18 \pm 0.01)R_V$ found by Whittet & van Breda (1978).

We interpret the correlation of $\lambda_{\max}(A_V = 0)$ with $\langle R_V \rangle$ as being due to the underlying differences in the total grain size distribution between the clouds and the (universal) slope in $\lambda_{\max}$ versus A_V as due to varying degrees of grain alignment at different depths into the clouds caused by a common mechanism.

The data indicate that the lack of aligned small grains at larger visual extinctions, indicated by large values of $\lambda_{\max}$, is due to loss of alignment rather than grain destructions. This can be seen by comparing $\lambda_{\max}$ as a function of $p_{\max}/A_V$ and of R_V. In Figure 15 we show $\lambda_{\max}$ for the Tycho screened lines of sight, adjusted to Chamaeleon, as functions of either the alignment efficiency ($p_{\max}/A_V$) or R_V. The adjustment performed here consists of subtracting the difference in derived $\lambda_{\max}(A_V = 0)$ between the cloud and that for Chamaeleon for the sight lines in each cloud (i.e., $\lambda^*_{\max} = \lambda_{\max} - [\lambda_{\max}(A_V = 0)^{\rm cloud} - \lambda_{\max}(A_V = 0)^{\rm Cham}]$).

A distinct anticorrelation (albeit, again, with outliers) is seen in the $\lambda_{\max}$ versus $p_{\max}/A_V$ (Fig. 15, *left panel*), indicating that as the relative number of aligned grains increases, the average size of the aligned grains decreases. No correlation is seen in the $\lambda_{\max}$ versus R_V plot (Fig. 15, *right panel*). Very similar plots, again, result if we instead use the *Hipparcos* screened sample.

As equation (1) shows, when all other parameters remain fixed, the smallest grains will have their rotation damped out by gas collisions the fastest. Hence, when we find that smaller and smaller grains remain aligned, either the damping is lessened or the driving mechanism for the spin-up is being enhanced. The correlations of $\lambda_{\max}$ with A_V show that as we get increasingly close to the cloud surface, smaller grains remain aligned. As has been shown on large scales for low radiation intensity cloud envelopes by Andersson & Wannier (1993) and Wannier et al. (1999) and recently on small scales in the higher radiation field case of the Horsehead Nebula by Habart et al. (2005), cloud envelopes show isobaric structures in the gas pressure, and hence equation (1) becomes

$$t_{\rm damping} \propto \frac{a\sqrt{T}}{P_{\rm gas}}, \quad (11)$$

with $P_{\rm gas}$ a constant for a given cloud.

Hence, an increase in temperature (assuming an isobaric equation of state) should lead to a decrease in $\lambda_{\max}$. We searched the literature for *Copernicus* and *FUSE* measurements of the

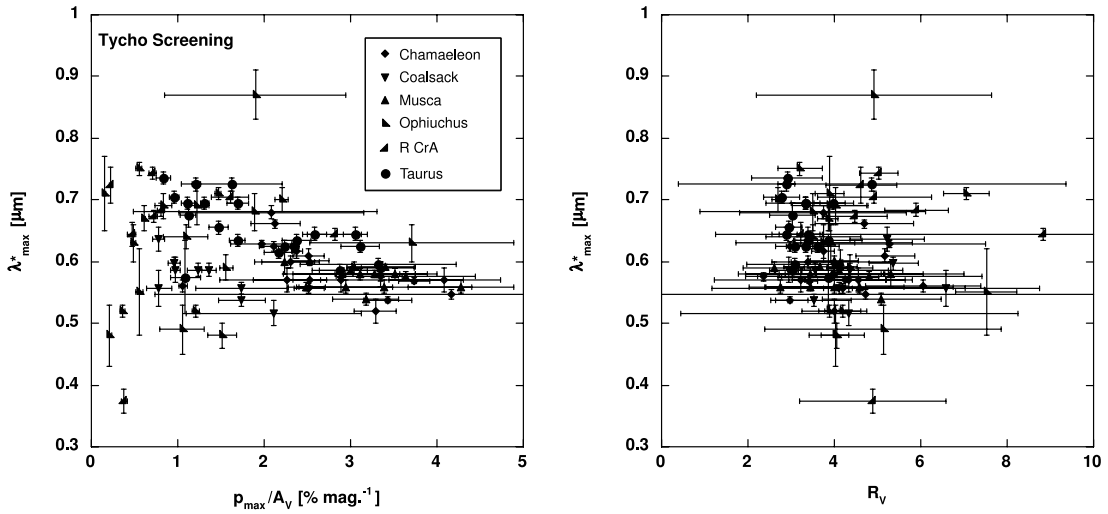

FIG. 15.—Adjusted location of the peak of the polarization curve shown as functions of alignment efficiency ($p_{\max}/A_V$; *left*) and R_V (*right*) for the Tycho screened sample. In both cases the measured $\lambda_{\max}$ has been adjusted to the Chamaeleon value by subtracting the difference in derived $\lambda_{\max}(A_V = 0)$ between the cloud and that for Chamaeleon for the sight lines in each cloud, i.e., $\lambda^*_{\max} = \lambda_{\max} - [\lambda_{\max}(A_V = 0)^{\rm cloud} - \lambda_{\max}(A_V = 0)^{\rm Cham}]$.

$J = 1/J = 0$ excitation temperature for the six clouds in our study. Unfortunately, only for Ophiuchus and Chamaeleon are there currently multiple interstellar sight lines published, and not all of those sight lines have been studied in polarimetry. For Ophiuchus, five sight lines were studied by Snow & Jenkins (1980), with an additional two by Cartledge et al. (2004). These yield a range in 1–0 temperatures of 46–90 K. For Chamaeleon, Gry et al. (2002) report 1–0 excitation temperatures for three stars between 60 and 66 K. Rachford et al. (2001) report $T = 63$ K for the line of sight toward HD 110432 behind the Coalsack. For the five Ophiuchus sight lines with H_2 data, measured $\lambda_{\max}$ can be extracted from Serkowski et al. (1975), while one of the Chamaeleon stars (HD 96675≡F24) and HD 110432 are included in the present data samples. In Figure 16 we plot both the measured values of $\lambda_{\max}$ and the offset from the best-fit relations in

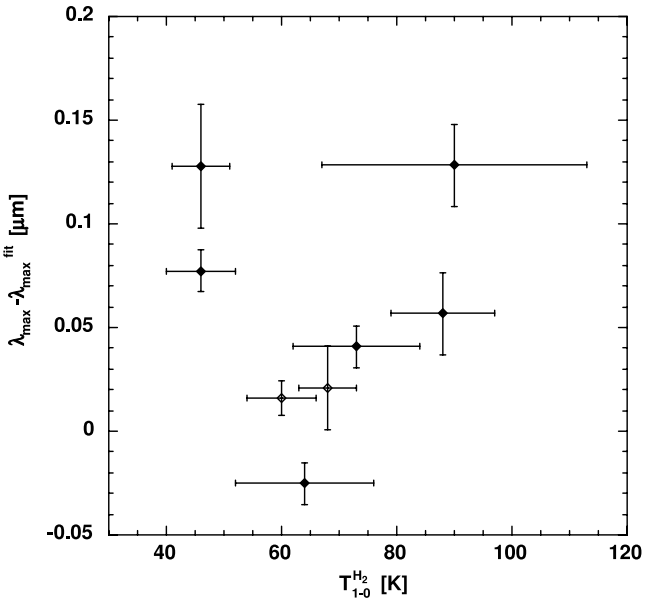

FIG. 16.—Offsets from the $\lambda_{\max}$ vs. A_V fits plotted as a function of the 1/0 H_2 temperatures for six stars in Ophiuchus (*filled diamonds*) and one each in Chamaeleon (*gray open diamond*) and the Coalsack (*black open diamond*). No correlation is evident.

$\lambda_{\max}$ versus A_V for each cloud. No clear correlation is apparent. We therefore conclude that variations in gas temperature are unlikely to explain the variations in the grain alignment.

Based on these observational results, we conclude that the data support grain alignment driven by the radiation field. This conclusion is consistent with recent developments in the theory of interstellar grain alignment. Several authors (Draine & Weingartner 1996; Weingartner & Draine 2003; Cho & Lazarian 2005) have shown that direct radiative torques are the theoretically most likely mechanism for explaining the spin-up of interstellar grains required to allow the magnetic alignment to take place.

We note, however, that our results cannot exclude alignment driven by molecular hydrogen formation (in steady state any formation of H_2 must be preceded by the radiative destruction of the molecule, and hence this mechanism is also more strongly active at smaller A_V values). Indeed, if we use the models of Kim & Martin (1995) to estimate the smallest aligned grains at the surface of the clouds, using $\lambda_{\max}(A_V = 0) \approx 0.5$ μm, we find that grains as small as 0.01–0.04 μm need to be at least partially aligned. For silicate grains in a diffuse cloud environment, Table 5 of Draine & Weingartner (1996) shows that for such small grains, H_2 formation driving is dominant over direct radiative torques. We note, however, that according to Lazarian & Draine (1999), VSGs should flip frequently due to Barnett and nuclear relaxation. Thus, under H_2 formation torques (fixed in the grain coordinate system) they are expected to become thermally trapped and not be able to achieve suprathermal spins. Further observational and theoretical studies are clearly needed to clarify the origin of the very small $\lambda_{\max}(A_V = 0)$ we observe.

4.3. *Influence of Star Formation*

Figure 11 indicates that the scatter in $\lambda_{\max}$ is related to the star formation activity of the cloud. We here explore a possible mechanism for this dependence, but we start by noting that turbulence, and its associated line-of-sight variations in the magnetic field direction, is not a likely cause. This is because $\lambda_{\max}$ is not, to first order, dependent on the absolute amount of polarization and because turbulence should affect the polarization in all bands similarly, leaving $\lambda_{\max}$ unaffected.

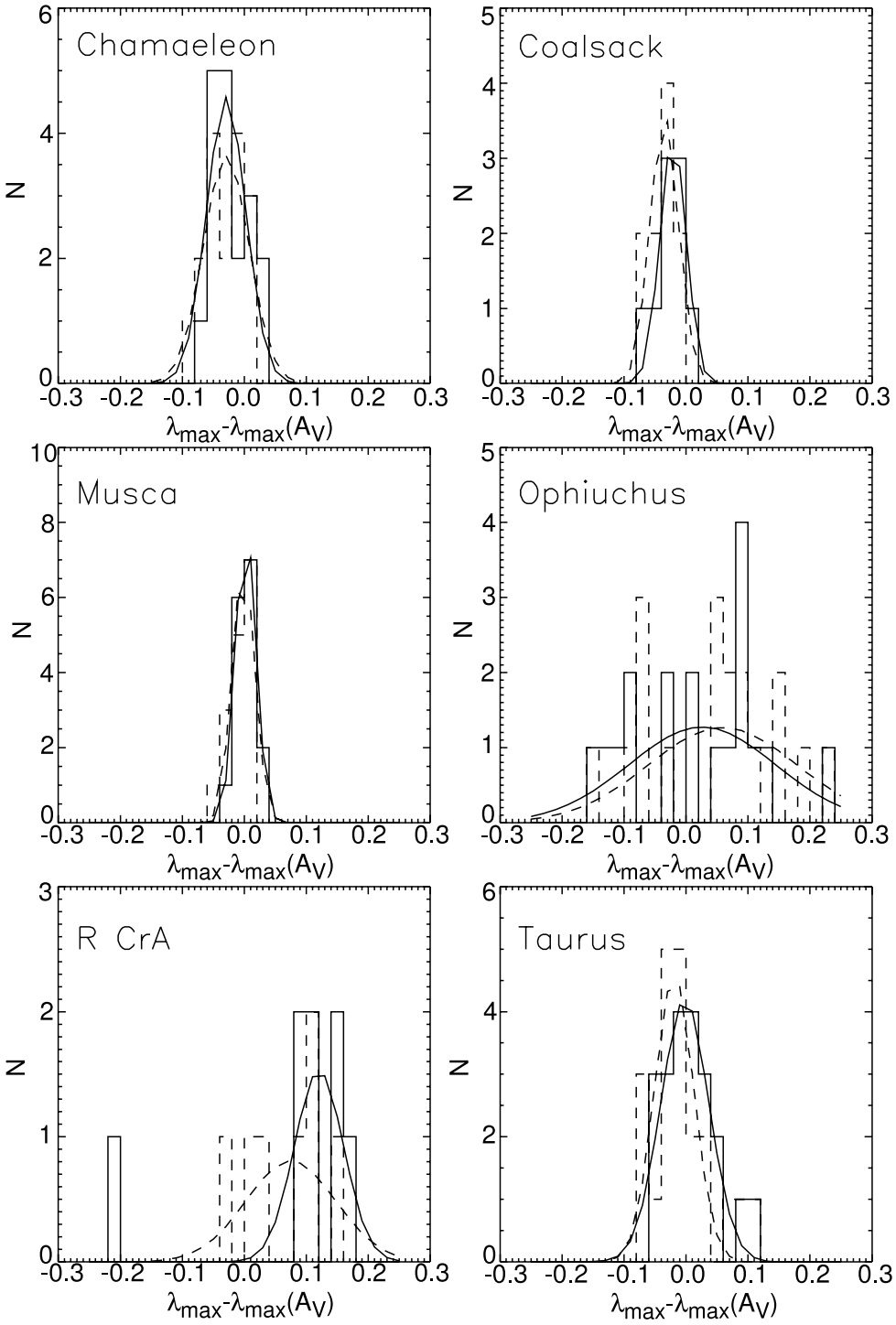

FIG. 17.—Offsets from the fits in λ_{max} vs. A_V shown in histogram form (solid histograms and lines for the Tycho screening, dashed histograms and lines for the *Hipparcos* screening). The offsets are from the universal slope relations.

In Figure 17 we show histograms of the distance from the best fits in λ_{max} with A_V for the six clouds using the "universal slope" relations. As is clear by a visual inspection, the scatter increases from the Coalsack, Chamaeleon, and Musca through Taurus to Ophiuchus and R CrA.

In Figure 18 we plot the scatter around the best fit in λ_{max} with A_V as a function of the "bright star fraction" [bsf (L^i_{bol})] of embedded YSOs. The bright star fraction is defined as the number fraction of objects brighter than a given bolometric luminosity (L^i_{bol}) to the total number of objects (cf. Chen et al. 1997). The error bars on the bsf's reflect counting statistics. The data for Chamaeleon, Ophiuchus, R CrA, and Taurus are taken from Chen et al. (1997). For the Coalsack, which does not show any star formation, we here use bsf $\equiv 0$. Musca has not been specifically studied for star formation activity although some T Tauri stars are detected in the general Chamaeleon-Musca complex (Mizuno et al. 1998). To separate the Coalsack and Musca points, we have for plotting purposes assigned a bsf of 0.17 midway between Chamaeleon and the Coalsack. Neither point was used in the fitting.

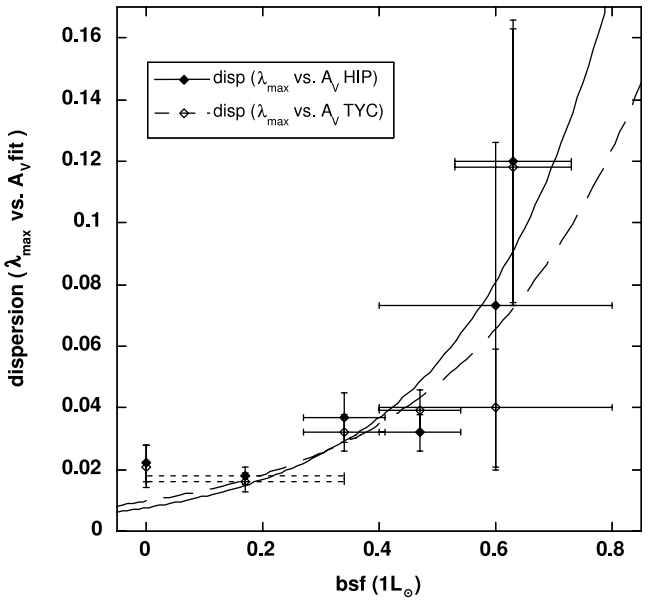

FIG. 18.—Scatter in the fit of λ_{max} vs. A_V plotted against the bright source fraction of the embedded YSOs (open symbols for the *Hipparcos* screened sample and filled diamonds for the Tycho screened sample). The lines are the best-fit exponentials.

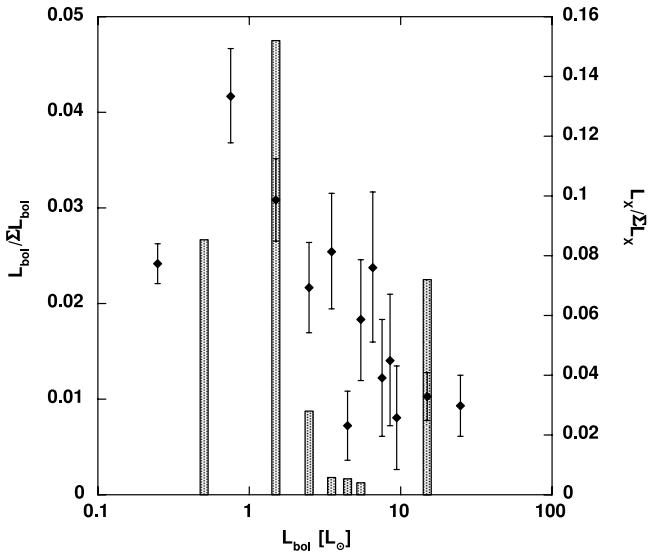

FIG. 19.—Combined binned fractional bolometric luminosity function of YSOs in Chamaeleon, Ophiuchus, and Taurus (*diamonds*; Chen et al. 1997). This shows the fraction of the total YSO luminosity, per unit luminosity, originating from a given subsample of YSOs. The binned fractional X-ray luminosity function of Ophiuchus YSOs is plotted as histograms. The binned fractional luminosity functions peak at $\sim$1–2 $L_\odot$.

We used power-law and exponential fits for several choices of the break point (L^i_{bol}; see above) in the bsf and find a best fit using an exponential for $L_{bol} = 1\ L_\odot$, yielding a correlation coefficient of $R = 0.88$ for the *Hipparcos* screened sample and 0.79 for the Tycho screened sample; the resulting fit is overplotted in Figure 18. At both smaller and larger L^i_{bol} the fit is worse. While not conclusive, this is consistent with an origin of the correlation due to the influence of the YSOs since the contribution, per unit luminosity range, to the total luminosity of the YSOs peaks around 1–2 $L_\odot$. This is illustrated in Figure 19, where we show the relative contribution to the bolometric and X-ray luminosity per unit L_{bol} for different subsamples. The data for the bolometric luminosity are a combination of the data for Chamaeleon, Ophiuchus, and Taurus, taken from Chen et al. (1995). The individual cloud data give similar results but with bigger scatter. The data for the X-ray luminosity are from Grosso et al. (2000). We chose a variable binning aimed at providing good resolution while collecting enough targets per bin to achieve reasonable statistics per bin. The relative binned bolometric luminosity peaks at $\sim$1 $L_\odot$ depending marginally on the exact binning, while the X-ray luminosity peaks at $\sim$1–2 $L_\odot$ with significant contributions from individual high-luminosity stars. (The 10–20 $L_\odot$ bin, however, only contains two stars. We have also excluded target A21 from Grosso et al. [2000] with $L_{bol} = 1100\ L_\odot$ and $\log L_X = 30.8$ in the plot.)

In Taurus (and R CrA if using the *Hipparcos* screening) the outliers in Figure 17 are primarily located on the positive side of the plots. Depending on whether we use the Tycho or *Hipparcos* based screenings, the data for R CrA show either a fairly wide dispersion or a significant offset in the center of the distribution. For Chamaeleon, the Coalsack, Musca, and Ophiuchus, the average of the distances of points from fits is much less than their associated standard deviation. Also for Taurus the average offset is smaller than the standard deviation, but here the distribution has a statistically significant positive skew (Press et al. 1986, p. 457) of 0.66 ± 0.53 for the *Hipparcos* screening and 0.57 ± 0.53 for the Tycho screening.

The scatter is likely due to porosity in the clouds, introduced by the effects of star formation, as seen in the dispersions between I_{60}/I_{100} versus A_V plots (Appendix). However, for variations in the radiation field intensity caused by cloud porosity alone we would expect the scatter to be symmetrical. Particularly for Taurus and R CrA we are thus led to consider possible mechanisms that will drive λ_{max} selectively to larger values, and hence also possible sources of additional, localized, grain rotation damping.

Given the ubiquity of X-ray emission from YSOs, it is worth considering what effects X-rays from the embedded YSOs would have on the grain rotation. One important X-ray–induced effect is the ejection of photoelectrons from the grains and both the subsequent heating of the gas and charging of the grains. As shown by Draine & Lazarian (1998), the dominant rotation damping mechanism in molecular cloud environments for VSGs (smaller than those discussed herein) is plasma drag due to the interaction between the ions in the gas and the electric dipole moment of the grain. Since the dipole moment of the grain is proportional to the grain charge (Draine & Lazarian 1998), enhanced localized grain charging would also mean enhanced localized rotation damping, in addition to the enhancement from gas heating. If we extrapolate the molecular cloud (MC) panel of Figure 4 of Draine & Lazarian (1998) to the 0.05 μm range, we find that in the nominal model, neutral gas drag is the dominant damping mechanism. However, plasma drag is only less important by a factor of a few. Hence, an increase in the grain charge by an order of magnitude would invert this relative importance. The typical X-ray ($h\nu \sim 0.5$–5 keV) luminosity of embedded YSOs is 10^{30}–10^{31} ergs s^{-1}, with flares reaching significantly higher (Ozawa et al. 2005; Grosso et al. 2000).

To derive a first-order estimate of whether X-rays from YSOs can significantly effect the grain rotation, we use the Ophiuchus cloud observations. In the observations of Grosso et al. (2000) for the inner part of the cloud, 66 targets were found within an approximate radius of 15′, or at a distance of 140 pc, 0.6 pc, yielding a characteristic projected source-to-source distance of

0.075 pc. At this radius the X-rays from a single source contribute an energy density of about $u = 5 \times 10^{-16}$ ergs cm^{-3}. Draine & Lazarian (1998) assumed an energy density in the radiation field of the 1% of the nominal ISRF for their molecular cloud medium, or $u \sim 9 \times 10^{-15}$ ergs cm^{-3} (Weingartner & Draine 2001). Taking into account also the contributions of far-ultraviolet emission from the YSOs, the high photoelectric yield at soft X-rays (Dwek & Smith 1996), and the contributions from the diffuse X-ray emission, likely caused by stellar winds (Ezoe et al. 2006), we feel that the influence of embedded X-ray sources is a viable cause of the localized rotation damping and warrants further study. However, observational studies and modeling, beyond the scope of the present paper, are required to quantify the importance of X-ray–induced grain rotation damping.

5. CONCLUSIONS

We have used new multiband polarimetry of the Southern Coalsack to study the alignment of interstellar grains. For this study the Coalsack has the advantage of not showing a systematic increase in the ratio of total to selective extinction, R_V, with increasing visual extinction and showing no star formation. The former allows us to break the degeneracy between increasing values of the wavelength of maximum polarization ($\lambda_{\rm max}$) due to the potentially lessened driving of the grain spin and due to grain growth. We find a tight correlation of $\lambda_{\rm max}$ with A_V over the limited range of $A_V = 1$–2.5, but with a significant amount of outliers. Using polarization data from the literature, together with archival FIR emission data, for an additional five nearby clouds, we show that the outliers in the $\lambda_{\rm max}$ versus A_V plot are primarily due to geometrical effects, causing the measured visual extinction to become a poor tracer of the extinction "seen" by the dust grains under study.

Screening the observations based on the I_{60}/I_{100} versus A_V relationship, we find that for clouds without, or with only low, star formation activity, $\lambda_{\rm max}$ is tightly correlated with A_V. We performed the screening based on two somewhat overlapping data sets, namely, field stars background to the clouds from either the *Hipparcos* catalog or the catalog of Tycho targets with known spectral classifications (Wright et al. 2003). Screening with the two field star samples yields consistent results but slightly different numerical parameters. In both cases, the correlation between $\lambda_{\rm max}$ and A_V shows a universal slope and zero-A_V intercepts proportional to the averages of R_V in the clouds, such that

$$\lambda_{\rm max} = (0.15 \pm 0.01)\langle R_V \rangle + (0.038 \pm 0.007) A_V \quad (12)$$

for the *Hipparcos*-based screening and

$$\lambda_{\rm max} = (0.15 \pm 0.01)\langle R_V \rangle + (0.028 \pm 0.005) A_V \quad (13)$$

for the Tycho-based screening, where we have imposed a zero intercept in the $\lambda_{\rm max}^{A_V=0}(\langle R_V \rangle)$ relation.

Within each cloud, we do not find correlations between $\lambda_{\rm max}$ and R_V.

We interpret the positive slope in $\lambda_{\rm max}$ versus A_V as evidence for radiation-induced grain spin-up. Our data cannot conclusively differentiate between direct radiative torques and H_2 formation torques. A possible role for the latter is, however, indicated by the small value of $\lambda_{\rm max}$ at $A_V = 0$, using the models by Kim & Martin (1995).

Compensating for the different $\lambda_{\rm max}(A_V = 0)$ between clouds, we find that $\lambda_{\rm max}$ is anticorrelated with the alignment efficiency, $p_{\rm max}/A_V$, further supporting the conclusion that the systematic variation in $\lambda_{\rm max}$ as a function of A_V is indeed due to grain alignment rather than changes in the grain size distribution.

The scatter around the $\lambda_{\rm max}$ versus A_V correlation, as well as the I_{60}/I_{100} versus A_V relationship, increases with the SFR in the cloud and is correlated with the number fraction of YSOs brighter than $1L_{\rm bol}$. In particular, for the R CrA and Taurus clouds the scatter shows asymmetries toward positive values, indicating possible evidence for localized enhancements in the grain rotation damping. The implied patchiness of the excess damping, together with the correlation of scatter in $\lambda_{\rm max}$ with bright YSOs and the high X-ray output of such embedded sources, leads us to propose a connection to photoelectric grain charging and associated plasma damping of the grain rotation.

Thus, to quantitatively understand interstellar polarization, we must know the strength of the radiation field at the location of the grain, as well as the star formation environment of the region, likely including the X-ray flux seen by the grain. Further surveys of the polarization curve for clouds with known SFRs, as well as significant numbers of well-characterized lines of sight at large ($A_V > 3$ mag) visual extinctions, both in the present sample of clouds and in new ones, would allow the results presented in this paper to be tested and extended. We are currently pursuing several such studies.

It is a pleasure to acknowledge many helpful discussions with Alex Lazarian, Joe Weingartner, and Bruce Draine. Kip Kuntz and Steve Drake provided helpful pointers to the X-ray properties of YSOs. The referees provided several suggestions and challenges that helped to significantly improve the paper. This research has made extensive use of the VizieR catalog access tool at CDS, Strasbourg, France, as well as of the NASA/IPAC Infrared Science Archive, operated by the Jet Propulsion Laboratory, California Institute of Technology, under contract with the National Aeronautics and Space Administration. B-G A. gratefully acknowledges travel support from the Center for Astrophysical Sciences at Johns Hopkins University.

APPENDIX

DOES THE 60 μm–TO–100 μm RATIO REALLY TRACE THE LOCAL RADIATION FIELD INTENSITY?

As noted in the introduction, several authors (e.g., Langer et al. 1989; Snell et al. 1989; Jarrett et al. 1989) have shown that the I_{60}/I_{100} ratio is anticorrelated with column density of CO and interpreted this as a temperature effect. However, as shown by, e.g., Bernard et al. (1993), the relative abundance of the VSGs decreases toward the center of clouds, and we therefore need to ascertain what part of the variations seen in the FIR ratios is dominated by grain heating rather than by abundance effects. First, we note that modern theories of the FIR emission (Draine & Li 2007) support the use of the I_{60}/I_{100} ratio as an irradiation tracer. Figure 12 of that paper shows a very small effect from the variation of the polycyclic aromatic hydrocarbon (PAH) fraction, while Figure 13 shows that the ratio is very sensitive to the strength of the radiation field.

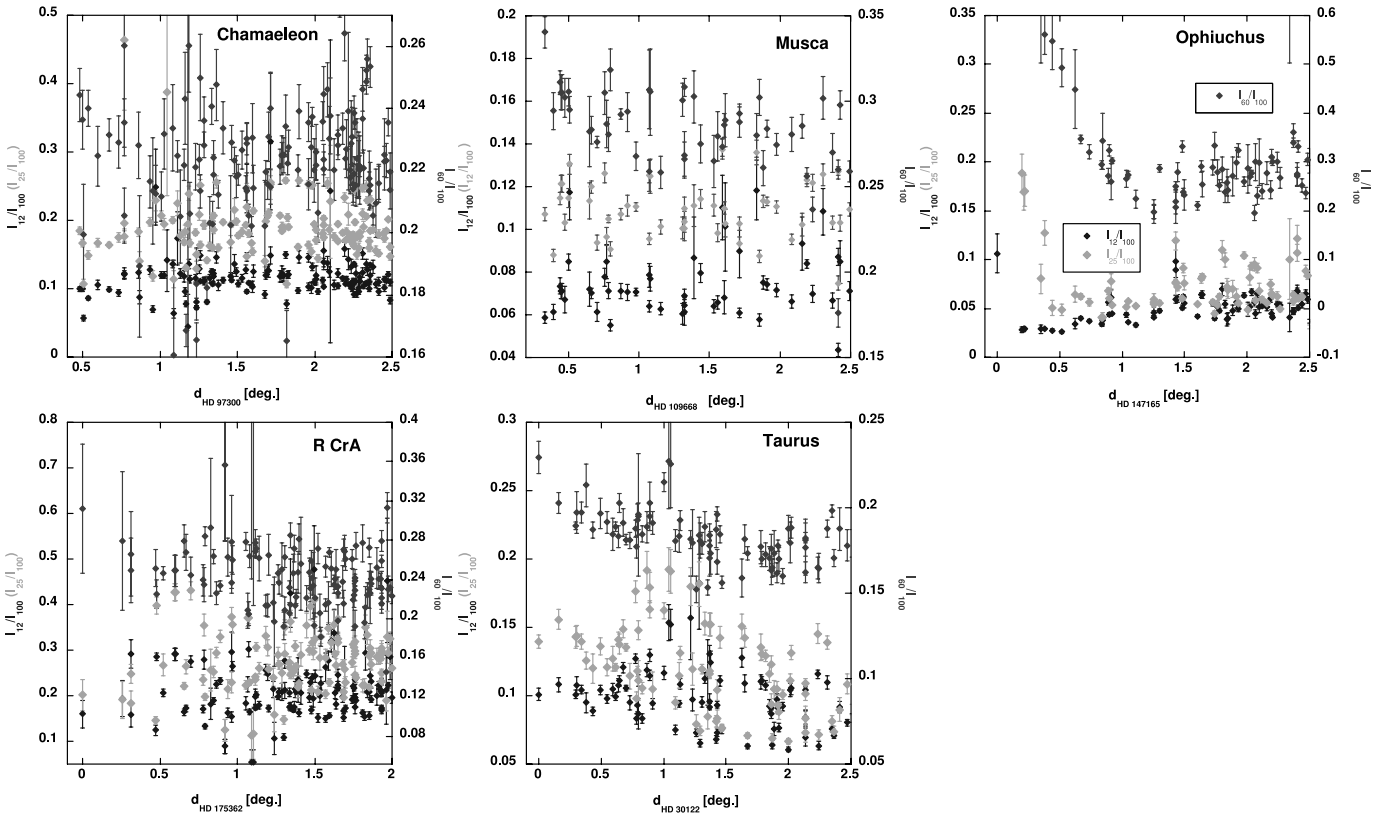

FIG. 20.—Ratios of I_{12}/I_{100} (*lower*), I_{25}/I_{100} (*middle*), and I_{60}/I_{100} (*upper*) are plotted for Chamaeleon, Musca, Ophiuchus, R CrA, and Taurus, against the on-the-sky distance to the dominant nearby hot star. As discussed in the main part of the text, the 60 μm–to–100 μm ratio responds noticeably to the presence of the hot, high-luminosity star. The 25 μm–to–100 μm ratio shows a smaller response, while the 12 μm–to–100 μm ratio shows very little response to the presence of the hot stars. This is consistent with an origin in dust heating through irradiation of the grains but would be difficult to explain in terms of changes in the relative abundances of the different grain populations. [*See the electronic edition of the Journal for a color version of this figure.*]

Arguing in somewhat more detail, the models by Desert et al. (1990) indicate that the 100 μm band emission is dominated by large grains with a minor contribution from the VSGs, while the 60 μm band contains a significant contribution from both large grains and the VSGs. The 25 μm band emission predominantly samples the VSGs (with some emission from PAHs), and the 12 μm band predominantly samples the PAHs with a contribution from the VSGs. Hence, if the variability in the FIR ratios is primarily driven by VSG abundance effects, the I_{25}/I_{100} ratio should show bigger deviations, whereas if the variability is primarily due to temperature variations, the I_{60}/I_{100} should be more affected. Also, if irradiation (and hence heating) dominates the FIR emission, we should be able to detect effects due to physically nearby hot stars on the dust in each cloud.

In Figure 20 we plot the ratios of I_{60}/I_{100}, I_{25}/I_{100}, and I_{12}/I_{100} as functions of the on-the-sky distance between the locations of the Tycho-selected field stars and early B stars located close to the clouds (Table 6). This figure shows both that the I_{60}/I_{100} responds to the enhanced radiation field caused by localized sources and that the I_{25}/I_{100} and I_{12}/I_{100} ratios show successively less effect from the enhanced radiation field.

Figure 21 shows the dispersions around the best fit in I_{60}/I_{100} versus A_V for the Tycho-selected field stars for the clouds in our study as a function of the bright star fraction for each cloud (we have here also added the result from an equivalent analysis of the Lupus I field). A clear correlation is seen, tightly fitted by a power-law function. This can be qualitatively understood in terms of variations in the local radiative heating of the dust in a porous medium where the porosity is due to the influence of newly formed stars.

TABLE 6
B STARS AFFECTING THE DUST

Cloud	Star	Spectral Class	V (pc)	d[a]
Chamaeleon	HD 97300	B9 V	9.0	188±36
Musca	HD 109668	B2 IV	2.7	94±4
Ophiuchus	σ Sco	B1 III	2.9	225±41
Ophiuchus	ρ Oph D	B3/4 V	6.8	136±25
R CrA	HD 175362	B3 V	5.4	130±16
Taurus	HD 30122	B5 III	6.3	216±34

[a] Based on *Hipparcos* trigonometric parallaxes.

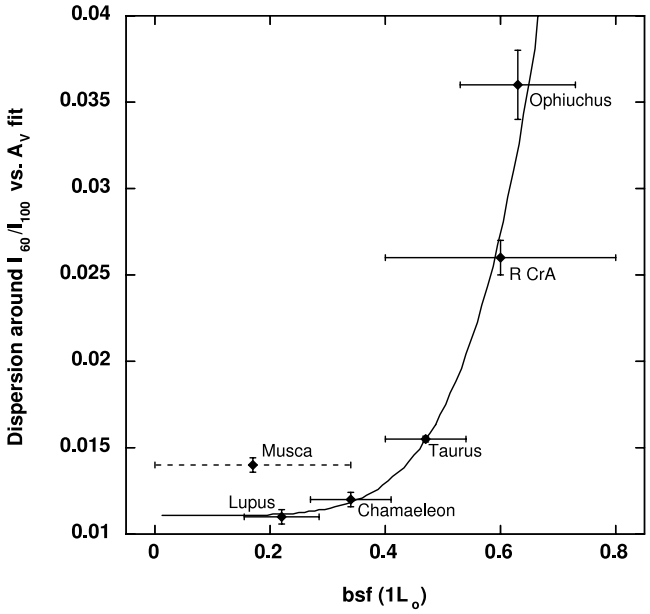

FIG. 21.—Dispersions around the best I_{60}/I_{100} fits (Fig. 8) using the Tycho-based screening plotted as a function of the bright star fraction for each cloud (we have also added the results for a similar analysis of the Lupus I cloud). A very well defined sequence is found, well fitted by a power-law function.

Finally, we must ask whether the field star samples provide accurate representations of the behavior of the dust sampled by the polarization targets. The field star samples are generally somewhat shallower than the polarization samples. However, as the bottom panels of Figure 8 show, once anomalous sight lines are excluded, the distributions of the field stars and polarization targets around the best-fit lines are very similar. Unfortunately, background stars with well-established spectral classifications and large visual extinctions are very rare. However, in Figure 22 we show the I_{60}/I_{100} versus A_V plot for Taurus, with the field stars from the water ice surveys of Murakawa et al. (2000) and Teixeira & Emerson (1999) added. Here the Tycho field stars are plotted as black circles with gray error bars, the polarization targets used by us as black diamonds (those found to be "anomalous sight lines" have been overplotted with crosses), sight lines with $\tau(H_2O) < 0.05$ as open diamonds, and those with $\tau(H_2O) > 0.1$ as filled diamonds. No qualitative change in I_{60}/I_{100} versus A_V is seen at the onset of water ice mantles. However, at the optical depth where the 60 and 100 μm intensities flatten out as a function of A_V (*inset*), the linear I_{60}/I_{100} versus A_V relation seems to break down, as would be expected if the I_{60}/I_{100} ratio was primarily driven by irradiation.

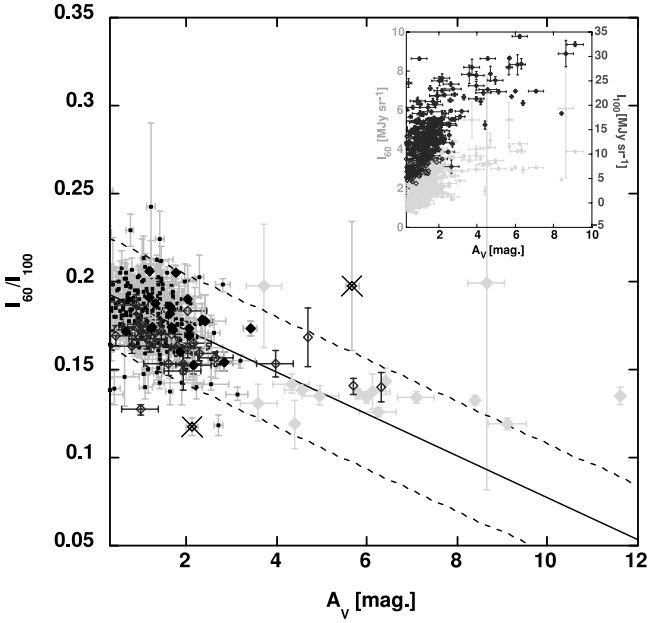

FIG. 22.—I_{60}/I_{100} vs. A_V plotted for Taurus, with the sight lines from Murakawa et al. (2000) and Teixeira & Emerson (1999) added. Black dots with gray error bars represent the Tycho field stars, black diamonds represent the polarization targets used in this paper (sight lines screened out as being anomalous are indicated with a cross), open diamonds represent sight lines with measured $\tau(H_2O) < 0.05$, and filled diamonds represent sight lines with measured $\tau(H_2O) > 0.1$. The inset shows the 60 and 100 μm intensities for each sight line. [*See the electronic edition of the Journal for a color version of this figure.*]

Together, these results lead us to conclude that we can indeed use the I_{60}/I_{100} ratio as a tracer of the strength of the radiation field seen by the dust grains. We note that we are not attempting to derive physical dust temperatures here, which, due to the complexity of the dust population, would not be reliable from a single ratio. We are simply using the FIR ratio as a tracer of the relative strength of the short-wavelength radiation in different parts of each cloud. In order to minimize any residual effects of variations in the grain size distribution, we additionally only use the FIR data to screen the visual extinction data for anomalous sight lines, as described in the main text.

REFERENCES

Andersson, B-G, Knauth, D. C., Snowden, S. L., Shelton, R. L., & Wannier, P. G. 2004, ApJ, 606, 341
Andersson, B-G, & Wannier, P. G. 1993, ApJ, 402, 585
Arnal, E. M., Morras, R., & Rizzo, J. R. 1993, MNRAS, 265, 1
Behr, A. 1959, Z. Astrophys., 47, 54
Bernard, J. P., Boulanger, F., & Puget, J. L. 1993, A&A, 277, 609
Bonnarel, F., et al. 2000, A&AS, 143, 33
Boulanger, F., Bronfman, L., Dame, T. M., & Thaddeus, P. 1998, A&A, 332, 273
Cambrésy, L. 1999, A&A, 345, 965
Cartledge, S. I. B., Lauroesch, J. T., Meyer, D. M., & Sofia, U. J. 2004, ApJ, 613, 1037
Chen, H., Grenfell, T. G., Myers, P. C., & Hughes, J. D. 1997, ApJ, 478, 295
Chen, H., Myers, P. C., Ladd, E. F., & Wood, D. O. S. 1995, ApJ, 445, 377
Cho, J., & Lazarian, A. 2005, ApJ, 631, 361
Codina-Landaberry, S., & Magalhaes, A. M. 1976, A&A, 49, 407
Covino, E., Palazzi, E., Penprase, B. E., Schwarz, H. E., & Terranegra, L. 1997, A&AS, 122, 95
Cox, A. N. 2000, Allen's Astrophysical Quantities (4th ed.; New York: AIP)
Cropper, M. 1985, MNRAS, 212, 709
Dachs, J., Kiehling, R., & Engels, D. 1988, A&A, 194, 167
Dachs, J., & Wamsteker, W. 1982, A&A, 107, 240
Davis, L. 1959, Z. Astrophys., 47, 59
Davis, L. J., & Greenstein, J. L. 1951, ApJ, 114, 206
Desert, F.-X., Boulanger, F., & Puget, J. L. 1990, A&A, 237, 215
Dolginov, A. Z., & Mitrofanov, I. G. 1976, Ap&SS, 43, 291
Draine, B. T., & Lazarian, A. 1998, ApJ, 508, 157
Draine, B. T., & Li, A. 2007, ApJ, 657, 810
Draine, B. T., & Weingartner, J. C. 1996, ApJ, 470, 551
Dwek, E., & Smith, R. K. 1996, ApJ, 459, 686
Ezoe, Y., Kokubun, M., Makishima, K., Sekimoto, Y., & Matsuzaki, K. 2006, ApJ, 638, 860
Gehrels, T. 1960, AJ, 65, 470
Grosso, N., Montmerle, T., Bontemps, S., André, P., & Feigelson, E. D. 2000, A&A, 359, 113
Gry, C., Boulanger, F., Nehmé, C., Pineau des Forêts, G., Habart, E., & Falgarone, E. 2002, A&A, 391, 675
Habart, E., Abergel, A., Walmsley, C. M., Teyssier, D., & Pety, J. 2005, A&A, 437, 177
Hall, J. S. 1949, Science, 109, 166
Hiltner, W. A. 1949a, Science, 109, 165
———. 1949b, ApJ, 109, 471
Hiltner, W. A., Garrison, R. F., & Schild, R. E. 1969, ApJ, 157, 313
Høg, E., et al. 2000, A&A, 355, L27
Houk, N., & Cowley, A. P. 1975, Michigan Catalogue of Two-dimensional Spectral Types for the HD Star (Ann Arbor: Univ. Michigan, Dept. of Astronomy)
Jarrett, T. H., Dickman, R. L., & Herbst, W. 1989, ApJ, 345, 881
Kenyon, S. J., Gomez, M., Marzke, R. O., & Hartmann, L. 1994, AJ, 108, 251
Kenyon, S. J., Lada, E. A., & Barsony, M. 1998, AJ, 115, 252
Kim, S.-H., & Martin, P. G. 1994, ApJ, 431, 783
———. 1995, ApJ, 444, 293
Kim, S.-H., Martin, P. G., & Hendry, P. D. 1994, ApJ, 422, 164
Langer, W. D., Wilson, R. W., Goldsmith, P. F., & Beichman, C. A. 1989, ApJ, 337, 355
Lazarian, A. 2003, J. Quant. Spectrosc. Radiat. Transfer, 79, 881
Lazarian, A., & Draine, B. T. 1999, ApJ, 520, L67
Lupton, R. 1993, Statistics in Theory and Practice (Princeton: Princeton Univ. Press)
Marraco, H. G., Vega, E. I., & Vrba, F. J. 1993, AJ, 105, 258
Mathis, J. S. 1986, ApJ, 308, 281
Metreveli, M. D. 1968, Abastumanskaia Astrofizika Obs. Bull., 38, 93
Miville-Deschênes, M.-A., & Lagache, G. 2005, ApJS, 157, 302
Mizuno, A., et al. 1998, ApJ, 507, L83
Murakawa, K., Tamura, M., & Nagata, T. 2000, ApJS, 128, 603
Naoi, T., et al. 2006, ApJ, 640, 373
Nesterov, V. V., Kuzmin, A. V., Ashimbaeva, N. T., Volchkov, A. A., Röser, S., & Bastian, U. 1995, A&AS, 110, 367
Ozawa, H., Grosso, N., & Montmerle, T. 2005, A&A, 429, 963
Press, W. H., Flannery, B. P., & Teukolsky, S. A. 1986, Numerical Recipes: The Art of Scientific Computing (Cambridge: Cambridge Univ. Press)
Purcell, E. M. 1979, ApJ, 231, 404
Racca, G., Gómez, M., & Kenyon, S. J. 2002, AJ, 124, 2178
Rachford, B. L., et al. 2001, ApJ, 555, 839
———. 2002, ApJ, 577, 221
Savage, B. D., Drake, J. F., Budich, W., & Bohlin, R. C. 1977, ApJ, 216, 291
Schmidt, G. D., Elston, R., & Lupie, O. L. 1992, AJ, 104, 1563
Seidensticker, K. J. 1989, A&AS, 79, 61
Seidensticker, K. J., & Schmidt-Kaler, T. 1989, A&A, 225, 192
Serkowski, K. 1968, ApJ, 154, 115
———. 1973, in IAU Symp. 52, Interstellar Dust and Related Topics, ed. J. M. Greenberg & H. C. van de Hulst (Dordrecht: Reidel), 145
Serkowski, K., Mathewson, D. L., & Ford, V. L. 1975, ApJ, 196, 261
Slutskij, V. E., Stalbovskij, O. I., & Shevchenko, V. S. 1980, Soviet Astron. Lett., 6, 397
Snell, R. L., Schloerb, F. P., & Heyer, M. H. 1989, ApJ, 337, 739
Snow, T. P., & Jenkins, E. B. 1980, ApJ, 241, 161
Straizys, V., Cernis, K., & Hayes, D. S. 1985, Ap&SS, 112, 251
Straizys, V., & Meistas, E. 1980, Acta Astron., 30, 541
Strömgren, B. 1956, AJ, 61, 354
Teixeira, T. C., & Emerson, J. P. 1999, A&A, 351, 292
Turnshek, D. A., Bohlin, R. C., Williamson, R. L., Lupie, O. L., Koornneef, J., & Morgan, D. H. 1990, AJ, 99, 1243
Ungerer, V., Nguyen-Quang-Rieu, Mauron, N., & Brillet, J. 1985, A&A, 146, 123
van der Werf, P. P., Dewdney, P. E., Goss, W. M., & vanden Bout, P. A. 1989, A&A, 216, 215
Vrba, F. J., Coyne, G. V., & Tapia, S. 1993, AJ, 105, 1010
Vrba, F. J., & Rydgren, A. E. 1984, ApJ, 283, 123
———. 1985, AJ, 90, 1490
Wannier, P., Andersson, B-G, Penprase, B. E., & Federman, S. R. 1999, ApJ, 510, 291
Wannier, P. G., Lichten, S. M., & Morris, M. 1983, ApJ, 268, 727
Weingartner, J. C., & Draine, B. T. 2001, ApJS, 134, 263
———. 2003, ApJ, 589, 289
Whittet, D. C. B. 1992, Dust in the Galactic Environment (Bristol: IOP)
Whittet, D. C. B., Gerakines, P. A., Carkner, A. L., Hough, J. H., Martin, P. G., Prusti, T., & Kilkenny, D. 1994, MNRAS, 268, 1
Whittet, D. C. B., Gerakines, P. A., Hough, J. H., & Shenoy, S. S. 2001, ApJ, 547, 872
Whittet, D. C. B., Kirrane, T. M., Kilkenny, D., Oates, A. P., Watson, F. G., & King, D. J. 1987, MNRAS, 224, 497
Whittet, D. C. B., & van Breda, I. G. 1978, A&A, 66, 57
———. 1980, MNRAS, 192, 467
Wilking, B. A., Lebofsky, M. J., Kemp, J. C., Martin, P. G., & Rieke, G. H. 1980, ApJ, 235, 905
Wilking, B. A., Lebofsky, M. J., & Rieke, G. H. 1982, AJ, 87, 695
Wright, C. O., Egan, M. P., Kraemer, K. E., & Price, S. D. 2003, AJ, 125, 359
Wurm, G., & Schnaiter, M. 2002, ApJ, 567, 370